




Bifurcation Graphs for the CR3BP via Symplectic Methods

On the Jupiter–Europa and Saturn–Enceladus systems

Agustin Moreno¹  · Cengiz Aydin¹ · Otto van Koert² · Urs Frauenfelder³ · Dayung Koh⁴

Accepted: 21 August 2024 / Published online: 19 November 2024

© The Author(s) 2024

Abstract

In this article, using the symplectic methods developed by Moreno and Frauenfelder (aimed at analyzing periodic orbits, their stability and their bifurcations), we will carry out numerical studies concerning periodic orbits in the Jupiter–Europa and Saturn–Enceladus systems. We will put emphasis on planar-to-spatial bifurcations, from deformation of the families in Hill’s lunar problem studied by Aydin. We will also provide an algorithm for the numerical computation of Conley–Zehnder indices, which are instrumental in practice for determining which families of orbits connect to which. As an application, we use our tools to analyze a well-known family of Halo orbits that approaches Enceladus at an altitude of 29 km, which bears interest for future space missions that visit the water plumes.

Keywords Symplectic geometry · Hamiltonian dynamics · Three-body problem · Space mission design · Bifurcations · Periodic orbits

✉ Agustin Moreno
agustin.moreno2191@gmail.com

Cengiz Aydin
cengiz.aydin@hotmail.de

Otto van Koert
okoert@snu.ac.kr

Urs Frauenfelder
urs.frauenfelder@math.uni-augsburg.de

Dayung Koh
dayung.koh@gmail.com

¹ Institut für Mathematik, Universität Heidelberg, Heidelberg, Germany

² Department of Mathematical Sciences, Seoul National University, Seoul, South Korea

³ Institut für Mathematik, Augsburg Universität, Augsburg, Germany

⁴ Pasadena, CA, USA

1 Introduction

Symplectic geometry is the branch of mathematics that studies the geometric properties of phase spaces, those spaces that describe the possible states of a classical physical system. It provides a proper framework to address problems in classical mechanics, e.g., the gravitational problem of N bodies in three-dimensional space (see e.g. [1–4] for reference textbooks). In the last 30 years, a host of theoretical tools have been developed in the field, with *Floer theory* as a notable example, whose emphasis is on the theoretical study of periodic orbits (see e.g. [5] and references therein).

In a more applied direction, periodic orbits are of interest for space mission design, as they model trajectories for spacecraft or satellites. Studying families of orbits aimed at placing a spacecraft around a target moon is relevant for space exploration, where optimizing over all possible trajectories is needed, in order to find ballistic orbits, avoid collisions, and maximize safety. In this context, the influence on a satellite of a planet with an orbiting moon can be approximated by a three-body problem of *restricted* type (i.e., the mass of the satellite is considered negligible by comparison). This is a classical problem which has been central to the development of symplectic geometry, and therefore it is not unreasonable to expect the modern available tools to provide insights. The need of organizing all information pertaining to orbits leads to the realm of data analysis, for which computationally cheap methods are important. The direction we will pursue is then encapsulated in the following questions:

Guiding questions

- **(Classification)** Can we tell when two orbits are *qualitatively different*?
 - **(Catalogue)** Can we resource-efficiently refine databases of known orbits?
 - **(Symplectic geometry)** Can we use methods from symplectic geometry to guide/organize the numerical work?
-

Here, we say that two orbits are *qualitatively different* if they cannot be joined by a regular family of orbits, i.e., a family which does *not* undergo bifurcation. The first two questions were addressed by the Moreno and Frauenfelder in [6], where the mathematical groundwork was developed, and obstructions to the existence of regular families were encoded in the topology of suitable quotients of the symplectic group. This method, whose main tool is the *GIT sequence*, gives a refinement of the well-known Broucke stability diagram [7]. This method was further developed for the case of Hamiltonian systems of arbitrary degrees of freedom by Moreno and Ruscelli in [8]. Frauenfelder, Koh and Moreno used it in combination with numerical work, addressing the third question [9]. In this article, we continue this line of research. As before, we have the following tools at our disposal.

Toolkit

- (1) **Floer numerical invariants** integers which stay invariant before and after a bifurcation, and so can help predict the existence of orbits, as well as being easy to implement. There is one invariant for arbitrary periodic orbits, and another for *symmetric* periodic orbits [9].
- (2) **The B-signs** [6] a \pm sign associated to each elliptic or hyperbolic Floquet multiplier of an orbit^a, which helps predict bifurcations. This is generalization of the classical Moser–Krein signature [10–12], which originally applies only to elliptic Floquet multipliers, to also include the case of hyperbolic multipliers, whenever the corresponding orbit is *symmetric*.
- (3) **Global topological methods:** the *GIT-sequence* [6], a sequence of spaces whose global topology encodes (and sometimes forces) bifurcations, and refines Broucke’s stability diagram [7] by adding the *B-signs*.
- (4) **Conley–Zehnder index** [13, 14] a winding number associated to each non-degenerate orbit, extracted from the topology of the symplectic group, which does not change unless a bifurcation occurs. It can be used to determine which families connect to which.

^aRecall that the Floquet multipliers of a closed orbit are by definition the non-trivial eigenvalues of the monodromy matrix

Both Jupiter–Europa and the Saturn–Enceladus systems are of tremendous current interest, within the context of future space missions. Works in the literature show that the continuation of out-of-plane bifurcations from basic families of planar periodic orbits, such as the direct (prograde) and retrograde ones, provides different regions of stability of three-dimensional motion around the smaller primary, see the work [15] on the Jupiter–Europa problem and [16] on systems of various mass ratios of interest. The first work describes also the Halo family, and the latter also investigated spatial connections between different planar direct orbits that branch out from period-doubling bifurcation, and observed that they are similar to those found in [17] for Hill’s lunar problem. Therefore, it is important to catalog as many planar and spatial periodic orbits as possible around the smaller primary, Europa and Enceladus, by starting from Hill’s lunar problem as a practical approach.

In this paper, we apply the symplectic toolkit in numerical studies of families of periodic orbits in the Saturn–Enceladus and the Jupiter–Europa system, by deformation of families in Hill’s lunar problem and their relations at bifurcation points studied by Aydin [18]. Our results illustrate the general principle that one may learn about a given system, by starting from known nearby systems, and then deforming. One of the highlights of our paper are bifurcation graphs relating various families of spatial orbits between triple cover of different direct and fifth cover of retrograde orbits (Figs. 16 and 19). We notice that one special connection between the direct and retrograde orbit in the Jupiter–Europa problem was already discussed in [15], and in [19] for higher order resonances; all the other branches we analyze, especially their CZ-indices with their interaction at bifurcation points, are novel.

Since its inception, index theory has been used in various forms in the study of bifurcations. Some examples of applications to celestial mechanics include [18, 20–22]. The typical strategy is to construct a family of orbits connecting the problem of interest to a situation which is analytically known. In this paper we propose a novel computational approach. We develop an algorithm that computes the index using

only locally available orbit information, bypassing the need to construct an entire family of orbits connecting to a previously known situation. In particular, this approach allows us to compute the CZ-index even when no family of orbits connecting to a previously known orbit is available. As a consequence, we can find bifurcations and hence new orbits by finding index jumps computationally. Based on the size of the index jump and the symmetries, we can also estimate the number of bifurcating orbits using the Floer theoretic invariants like the ones described Sect. 2.4. An additional practical advantage of this approach is that bifurcations can be detected without getting close to a degeneracy. Technically, the algorithm is achieved by a constructive approach to the symplectic path extension problem using the Iwasawa decomposition and the singular value decomposition to improve numerical stability. Details are given in Sect. 3.

We apply our method to various orbits in the Saturn-Enceladus system. In particular, in Appendix A, we apply these methods in order to analyze a family of Halo orbits in the Saturn-Enceladus system. This family approaches the plumes at an altitude of 29 km, and therefore may be used for future missions. As an illustration of the procedure sketched in the previous paragraph, we have applied our algorithm to detect a bifurcation of the sevenfold cover of the Halo orbit by computing index jumps. The resulting periodic orbit coming out of the sevenfold cover is shown in Fig. 23 of Appendix A and approaches Enceladus at an altitude of 14 km. Our novel tools were instrumental for our results.

2 Preliminaries

In this section, we review the toolkit. But first, we set up some language and notation. We refer the reader to [9] for details on the global topological methods.

2.1 Basic Notions

Mechanics/symplectic geometry Given a $2n$ -dimensional phase-space M with its symplectic form ω , a Hamiltonian function $H : M \rightarrow \mathbb{R}$, with Hamiltonian flow $\phi_t^H : M \rightarrow M$ which preserves ω (i.e., $(\phi_t^H)^* \omega = \omega$), and a periodic orbit x , the *monodromy matrix* of x is $M_x = D\phi_T^H$, where T is the period of x . Then M_x is a symplectic $2n \times 2n$ -matrix; we denote by $Sp(2n)$ the space of such matrices (the *symplectic group*). Given a periodic orbit x , its k -fold cover x^k is defined via $x^k(t) = x(k \cdot t)$ (i.e. x^k is x traversed k times).

Note that if H is time-independent then 1 appears twice as a *trivial* eigenvalue of M_x . We can ignore these if we consider the *reduced* monodromy matrix $M_x^{red} \in Sp(2n - 2)$, obtained by fixing the energy and dropping the direction of the flow.

- A *Floquet multiplier* of x is an eigenvalue of M_x , which is not one of the trivial eigenvalues (i.e., an eigenvalue of M_x^{red}).
- An orbit is *non-degenerate* if 1 does not appear among its Floquet multipliers.

- An orbit is *stable* if all its Floquet multipliers are semi-simple and lie on the unit circle.

We will only consider the cases $n = 2$ (planar problems) and $n = 3$ (spatial problems).

If M_x is symplectic, and $\mu \in \mathbb{C}$ is an eigenvalue of M_x , then so are $\bar{\mu}, 1/\mu, 1/\bar{\mu}$. Then we have the following cases:

- (\mathcal{P} , **parabolic**) $\mu = \pm 1$, in which case it has even multiplicity;
- (\mathcal{E} , **elliptic**) $|\mu| = 1$, in which case it comes as an elliptic pair $\mu, \bar{\mu} = 1/\mu$;
- (\mathcal{H}^+ , **positive hyperbolic**) $\mu \in \mathbb{R}, \mu > 0, \mu \neq 1$, in which case both $\mu, 1/\mu$ are positive;
- (\mathcal{H}^- , **negative hyperbolic**) $\mu \in \mathbb{R}, \mu < 0, \mu \neq -1$, in which case both $\mu, 1/\mu$ are negative;
- (\mathcal{N} , **complex/nonreal quadruple**) $\mu \notin S^1 \cup \mathbb{R}$, in which case it comes in a quadruple $\mu, \bar{\mu}, 1/\mu, 1/\bar{\mu}$.

Symmetries An *anti-symplectic involution* is a map $\rho : M \rightarrow M$ satisfying $\rho^2 = id$ and $\rho^* \omega = -\omega$. Its *fixed-point locus* is $fix(\rho) = \{x : \rho(x) = x\}$. An anti-symplectic involution ρ is a *symmetry* of the system if $H \circ \rho = H$. A periodic orbit x is *symmetric* if $\rho(x(-t)) = x(t)$ for all t . The *symmetric points* of the symmetric orbit x are the two intersection points of x with $fix(\rho)$. The (reduced or unreduced) monodromy matrix of a symmetric orbit at a symmetric point is a *Wonenburger* matrix:

$$M_x = M_{A,B,C} = \begin{pmatrix} A & B \\ C & A^T \end{pmatrix} \in Sp(2n), \tag{2.1}$$

where

$$B = B^T, \quad C = C^T, \quad AB = BA^T, \quad A^T C = CA, \quad A^2 - BC = id,$$

equations which ensure that M_x is symplectic. The eigenvalues of M_x are determined by those of the first block A [6]:

- If λ is an eigenvalue of M_x then its stability index $a(\lambda) = \frac{1}{2}(\lambda + 1/\lambda)$ is an eigenvalue of A .
- If a is an eigenvalue of A then $\lambda(a) = a + \sqrt{a^2 - 1}$ is an eigenvalue of M_x .

2.2 B-Signs

Assume $n = 2, 3$. Let x be a symmetric orbit with monodromy $M_{A,B,C}$ at a symmetric point. Assume a is a real, simple and nontrivial eigenvalue of A (i.e., $\lambda(a)$ is elliptic or hyperbolic). Let v be an eigenvector of A^T with eigenvalue a , i.e., $A^T v = a \cdot v$. The *B-sign* of $\lambda(a)$ is

$$\epsilon(\lambda(a)) = \text{sign}(v^T Bv) = \pm,$$

where B is as in Eq. (2.1). One easily sees that this is independent of v , and the basis chosen to write down the monodromy matrix. Note that if $n = 2$, we have two B -signs ϵ_1, ϵ_2 , one for each symmetric point; and if $n = 3$, we have two *pairs* of B -signs $(\epsilon_1^1, \epsilon_2^1), (\epsilon_1^2, \epsilon_2^2)$, one for each symmetric point and each eigenvalue.

Frauenfelder and Moreno have recently shown that a planar symmetric orbit is negative hyperbolic iff the B -signs of its two symmetric points differ [23]. One can define the C -signs similarly, obtained by replacing the B -block, with the C -block of M , and A^T , by A .

2.3 Conley–Zehnder Index

The CZ-index is part of the index theory of the symplectic group. It assigns a winding number to non-degenerate orbits. In practical terms, it helps understand which families of orbits connect to which (CZ-index stays constant if no bifurcation occurs, and jumps under bifurcation as shown in Fig. 1). It may be defined as follows.

Planar case Let $n = 2$, x planar orbit with (reduced) monodromy M_x^{red} , and x^k its k -fold cover which we assume to be non-degenerate for all $k \geq 1$.

- **Elliptic case** M_x^{red} is conjugated to a rotation,

$$M_x^{red} \sim \begin{pmatrix} \cos \varphi & -\sin \varphi \\ \sin \varphi & \cos \varphi \end{pmatrix}, \tag{2.2}$$

with Floquet multipliers $e^{\pm i\varphi}$. Here, φ is the rotation angle. Then

$$\mu_{CZ}(x^k) = 1 + 2 \cdot [k \cdot \varphi / 2\pi]$$

In particular, it is odd, and jumps by ± 2 if the eigenvalue 1 is crossed in a family.

Recall from (2.1) that for symmetric periodic orbits we have $M_x^{red} = \begin{pmatrix} a & b \\ c & a \end{pmatrix}$.

from elliptic to positive hyperbolic

from positive hyperbolic to elliptic

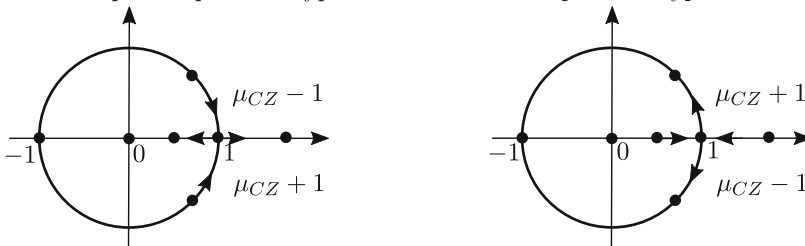


Fig. 1 μ_{CZ} jumps by ± 1 when crossing 1, according to direction of bifurcation, as shown. If it stays elliptic, the jump is by ± 2 . This is determined by the B -sign

Moreover, in view of (2.2) if $b < 0$ then the rotation is determined by φ and if $b > 0$ then the rotation is determined by $-\varphi$; this determines the CZ-index jump, see Fig. 1.

- **Hyperbolic case** M_x^{red} is diagonal up to conjugation,

$$M_x^{red} \sim \begin{pmatrix} \lambda & 0 \\ 0 & 1/\lambda \end{pmatrix},$$

with Floquet multipliers $\lambda, 1/\lambda$. Then

$$\mu_{CZ}(x^k) = k \cdot n,$$

where $D\phi_t^H$ rotates the eigenspaces by angle $\frac{\pi nt}{T}$, with n even/odd if x positive/negative hyperbolic. Notice that for symmetric periodic orbits the signatures of b and c are equal.

Note that in both cases above, in order to compute the CZ-index via the above formulae, we need to know the linearized flow along the *whole* of the orbit. That is, what matters is the path connecting the identity to the monodromy matrix, obtained by linearizing at any point of the orbit, and performing a full turn around the orbit. In the elliptic case, the rotation angle φ is then computed as a real number, and *not* modulo 2π , as it counts the number of rotations of the linearized flow along the whole periodic orbit.

Spatial case Let $n = 3$. Assume that the reflection along the xy -plane gives rise to a symplectic symmetry of H (e.g., the 3BP). If $x \subset \mathbb{R}^3$ is a planar orbit, then we have a symplectic splitting into planar and spatial blocks

$$M_x^{red} \sim \begin{pmatrix} M_p^{red} & 0 \\ 0 & M_s \end{pmatrix} \in Sp(4), \quad M_p^{red}, M_s \in Sp(2).$$

Then

$$\mu_{CZ}(x) = \mu_{CZ}^p(x) + \mu_{CZ}^s(x),$$

where each summand corresponds to M_p^{red} and M_s respectively. We have that

- Planar to planar bifurcations correspond to jumps in μ_{CZ}^p .
- Planar to spatial bifurcations correspond to jumps of μ_{CZ}^s .

A general definition of the CZ-index will be given in Sect. 3, which provides a direct way to numerically compute the CZ-indices. The computations of CZ-indices of families can also be carried out by not directly on the definition, but rather on determining them analytically for special families if these are known (e.g., in the

Kepler problem), and then determining the jumps at bifurcations arising after deformation, for which the B -signs are necessary, as explained above. This was the approach used by Aydin in [18, 22].

2.4 Floer Numerical Invariants

Recall that bifurcations occurs when studying families $c \mapsto x_c$ of periodic orbits, as a mechanism by which at some parameter time $c = c_0$ the orbit x_{c_0} becomes degenerate, and several new families may bifurcate out of it; see Fig. 2. The Floer numbers are meant to give a simple test to keep track of all new families. We will first need the following technical definition: a periodic orbit $x = y^k$, where y is its underlying simple orbit, is *bad* if k is even and

$$\mu_{CZ}(x) \not\equiv \mu_{CZ}(y) \pmod{2}.$$

Otherwise, it is *good*. In fact, a planar orbit is bad iff it is an even cover of a negative hyperbolic orbit (i.e. of the form x^k with k even, and x negative hyperbolic). And a spatial orbit is bad iff it is an even cover of either an elliptic-negative hyperbolic or a positive-negative hyperbolic orbit. Note that a good planar orbit can be bad if viewed in the spatial problem.¹

Given a bifurcation at a (degenerate) periodic orbit x , the *SFT-Euler characteristic* (or the *Floer number*) of x is

$$\chi(x) = \sum_i (-1)^{\mu_{CZ}^{i,bef}} = \sum_j (-1)^{\mu_{CZ}^{j,aft}}$$

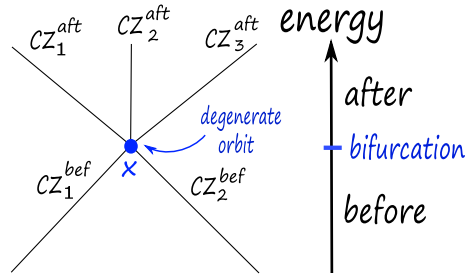
The sum on the left hand side is over **good** orbits *before* bifurcation, and right hand side is over **good** orbits *after* bifurcation, and $\mu_{CZ}^{i,bef/aft}$ denotes the corresponding CZ-indices. As these numbers only involve the parity of the CZ-index, one has simple formulas which bypass the computation of this index, as they only involve the Floquet multipliers:

- **Planar case** $\chi(x) = \#\{\text{good } \mathcal{H}^+\} - \#\{\mathcal{E}, \mathcal{H}^-\}.$
- **Spatial** **case**
 $\chi(x) = \#\{\mathcal{H}^{--}, \mathcal{E}\mathcal{H}^-, \mathcal{E}^2, \text{good } \mathcal{H}^{++}, \mathcal{N}\} - \#\{\mathcal{H}^{+-}, \text{good } \mathcal{E}\mathcal{H}^+\}.$

Here, \mathcal{E} denotes *elliptic*, \mathcal{H}^\pm denotes *positive/negative hyperbolic*, and \mathcal{N} denotes *nonreal* quadruples $\lambda, 1/\lambda, \bar{\lambda}, 1/\bar{\lambda}$. The above simply tells us which type of orbit

¹ While the terminology of good/bad orbits is perhaps an unfortunate use of language, it is widely used in the symplectic literature. For the purposes of this article, the theoretical reason why “good” orbits are better than the “bad” ones is that they are the ones that need to be counted in order to obtain invariance. But “bad” orbits might be conceivably good for the purposes of space mission design. Typical examples of bad periodic orbits are double covers of negative hyperbolic orbits appearing in period doubling bifurcations.

Fig. 2 A sketch of a bifurcation at a degenerate orbit, with the before/after orbits determined by the deformation parameter (the energy), each branch with its own CZ-index. The Floer number is a signed count of orbits which stays invariant



comes with a plus or a minus sign (the formula should be interpreted as either before or after).

Invariance The fact that the sums agree before and after—invariance—follows from deep results from *Floer theory* in symplectic geometry.² We will accept this as a fact, and use it as follows:

The Floer number can be used as a **test**: if the sums do *not* agree, we know the algorithm missed an orbit.

The invariant above works for arbitrary periodic orbits. There is a similar Floer invariant for *symmetric* orbits [9].

2.5 Global Topological Methods

These methods encode: bifurcations; stability; eigenvalue configurations; obstructions to existence of regular families; and *B*-signs, in a visual and resource-efficient way. The main tool is the *GIT sequence* [6], a refinement of the Broucke stability diagram via implementing the *B*-signs. This is a sequence of three branched spaces (or *layers*), together with two maps between them, which collapse certain branches together. Each branch is labeled by the *B*-signs. A symmetric orbit gives a point in the top layer, and an arbitrary orbit, in the middle layer. The base layer is \mathbb{R}^n (the space of coefficients of the characteristic polynomial of the first block of $M_{A,B,C}$). Then a family of orbits gives a path in these spaces, so that their topology encodes valuable information. The details are as follows.

GIT sequence: 2D Let $n = 2$, λ eigenvalue of $M^{red} \in Sp(2)$, with stability index $a(\lambda) = \frac{1}{2}(\lambda + 1/\lambda)$. Then $\lambda = \pm 1$ iff $a(\lambda) = \pm 1$; λ positive hyperbolic iff $a(\lambda) > 1$; λ negative hyperbolic iff $a(\lambda) < -1$; and λ elliptic (stable) iff $-1 < a(\lambda) < 1$. The Broucke stability diagram is then simply the real line, split into three components; see Fig. 3. If two orbits lie in different components of the diagram, then one should expect bifurcations in any family joining them, as the topology of the diagram implies that any path between them has to cross the ± 1 eigenvalues.

² For generic families of Hamiltonians on 4-dimensional phase spaces this can alternatively be proved by the using the normal forms of Meyer [24]. See for instance the Appendix in [9].

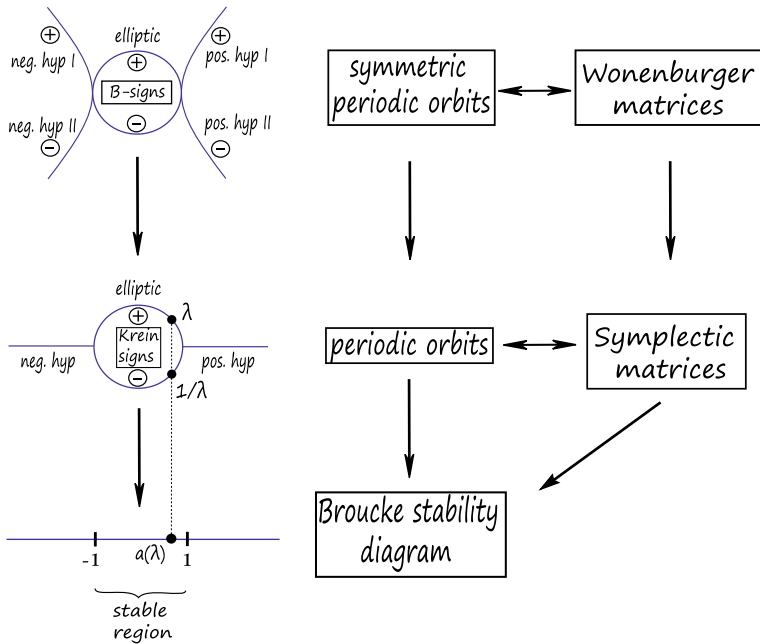


Fig. 3 The 2D GIT sequence. One obtains more refined information for symmetric orbits

One can think that the stability index “collapses” the two elliptic branches in the middle layer of Fig. 3 together. These two branches are distinguished by the B -signs, coinciding with the Krein signs [10, 11]. There is an extra top layer for symmetric orbits, where now each hyperbolic branch separates into two, and there is a collapsing map from the top to middle layer. Note that to go from one branch to the other, the topology of the layer implies that the eigenvalue 1 needs to be crossed. This means that one should expect bifurcations in any (symmetric) family joining them, *even if* they project to the same component of the Broucke diagram. To sum up:

- B -signs “separate” hyperbolic branches, for symmetric orbits
- If two points lie in different components of the Broucke diagram, one should expect bifurcation in any path joining them
- If two points lie in the same component of the Broucke diagram, but if B -signs differ, one should *also* expect bifurcation in any path joining them

GIT sequence: 3D Let $n = 3$. Given $M^{red} = M_{A,B,C} \in Sp(4)$, its *stability point* is $p = (\text{tr}(A), \det(A)) \in \mathbb{R}^2$. The plane splits into regions corresponding to the eigenvalue configuration of M^{red} , as in Fig. 4. The GIT sequence [6] adds two layers to this diagram, as shown in Fig. 5. The top layer has two extra branches than the middle one, for each hyperbolic eigenvalue.

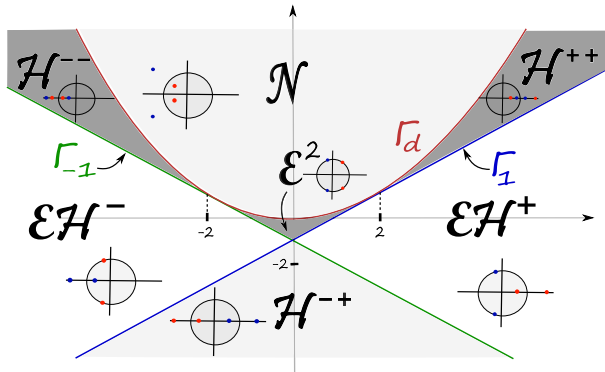


Fig. 4 The 3D Broucke stability diagram. Here, $\Gamma_{\pm 1}$ corresponds to eigenvalue ± 1 , Γ_d to double eigenvalue, \mathcal{E}^2 to doubly elliptic (stable region), and so on [6]

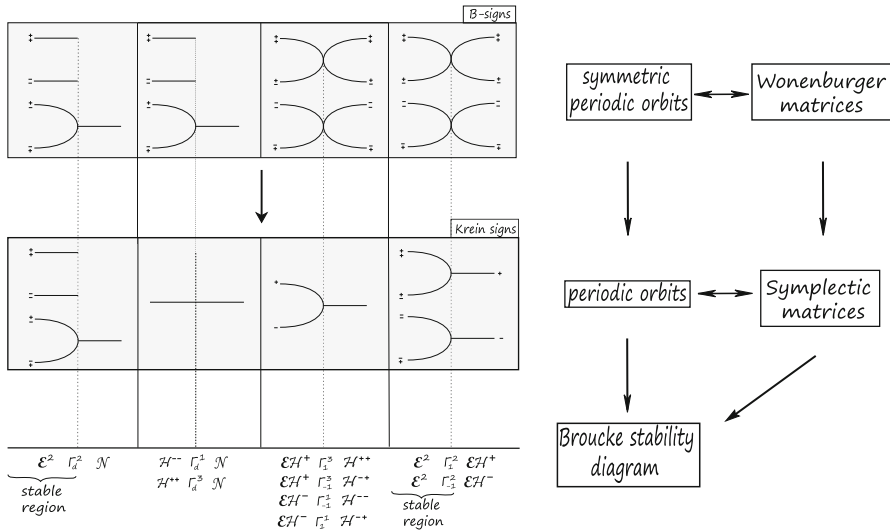


Fig. 5 The branches (represented as lines) are two-dimensional, and come together at the 1-dimensional “branching locus” (represented as points), where we cross from one region to another of the Broucke diagram

Bifurcations in the Broucke diagram An orbit family $c \mapsto x_c$ gives a path $c \mapsto p_c \in \mathbb{R}^2$ of stability points. The family bifurcates if p_c crosses Γ_1 . More generally, let Γ_φ^e be the line with slope $\cos(2\pi\varphi) \in [-1, 1]$ tangent to $\Gamma_d = \{y = x^2/4\}$, corresponding to matrices with eigenvalue $e^{2\pi i\varphi}$; and Γ_λ^h the tangent line with slope $a(\lambda) \in \mathbb{R} \setminus [-1, 1]$, corresponding to matrices with eigenvalue λ .

A k -fold bifurcation happens when crossing $\Gamma_{l/k}^c$ for some l

That is, higher order bifurcations are encoded by a pencil of lines tangent to a parabola, as in Fig. 6.

Example: symmetric period doubling bifurcation We finish this section with an example where our invariants give new information. Consider a symmetric orbit x going from elliptic to negative hyperbolic. A priori there could be two bifurcations, one for each symmetric point (B or C in Fig. 7). However, invariance of $\chi(x^2)$ implies only *one* can happen (note x^2 is *bad*). And where the bifurcation happens is determined by the B -sign, occurring at the symmetric point in which the B -sign does *not* jump; or alternatively, where the C -sign jumps.

2.6 Circular Restricted Three-Body Problem

The Circular Restricted Three-Body Problem (CRTBP) shown in Fig. 8 describes the motion of an infinitesimal mass with two primaries under mutual gravitational attraction. A dimensionless rotating coordinate system $(X^R - Y^R - Z^R)$ is defined at the barycenter of the two primaries with respect to the inertial frame $(X^I - Y^I - Z^I)$, rotating about Z^I with true anomaly v .

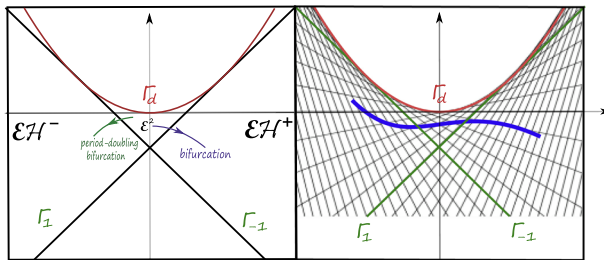


Fig. 6 Bifurcations are encoded by a pencil of lines

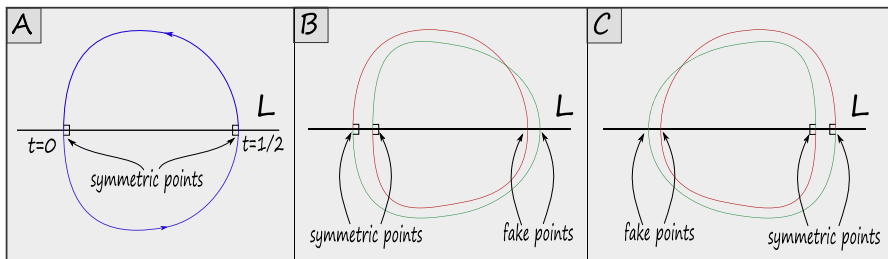
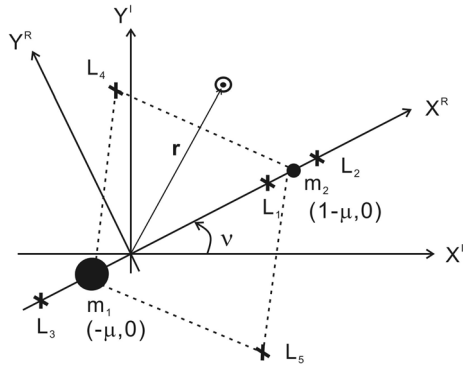


Fig. 7 Symmetric period doubling bifurcation. The *fake* symmetric points, while close to intersection points, do *not* intersect the fixed-point loci

Fig. 8 A schematic CRTBP configuration showing $x_1 = m_1$, $x_2 = m_2$, and two of the libration points in a non-dimensional rotating coordinate system $X^R - Y^R$, $Z^R(Z^I)$ are in the out-of-plane direction



The X -axis of the rotating coordinate system is aligned with the vector from the larger primary body (m_1) to the second primary body (m_2). The Z -axis is perpendicular to the primaries' orbital plane, and the Y -axis completes the right-handed coordinate system. The position vector \mathbf{r} points from the barycenter to the spacecraft in the rotating frame. The non-dimensional mass of the second primary is defined as

$$\mu = \frac{m_2}{m_1 + m_2} = m_2,$$

and then the larger body's mass is

$$1 - \mu = \frac{m_1}{m_1 + m_2} = m_1.$$

Define the unit of time so that the mean motion of the primary orbit is 1. Then the equations of motion for the infinitesimal mass is written as

$$\begin{aligned} \ddot{x} &= 2\dot{y} + x - (1 - \mu)\frac{x + \mu}{r_1^3} - \mu\frac{x - 1 + \mu}{r_2^3} \\ \ddot{y} &= -2\dot{x} + y - (1 - \mu)\frac{y}{r_1^3} - \mu\frac{y}{r_2^3} \\ \ddot{z} &= -(1 - \mu)\frac{z}{r_1^3} - \mu\frac{z}{r_2^3} \end{aligned}$$

where $r_1^2 = (x + \mu)^2 + y^2 + z^2$, $r_2^2 = (x - 1 + \mu)^2 + y^2 + z^2$. No closed form general solution is possible for the model. See e.g. [25].

The Hamiltonian describing the CRTBP is given by

$$\begin{aligned} H &: (\mathbb{R}^3 \setminus \{P_1, P_2\}) \times \mathbb{R}^3 \rightarrow \mathbb{R}, \\ H(q, p) &= \frac{1}{2} \|p\|^2 - \frac{\mu}{\|q - P_2\|} - \frac{1 - \mu}{\|q - P_1\|} + p_1 q_2 - p_2 q_1, \end{aligned}$$

where $q = (q_1, q_2, q_3)$ is the position of a satellite, $p = (p_1, p_2, p_3)$ is its momentum,

the mass of the secondary body m_2 is fixed at $P_2 = (1 - \mu, 0, 0)$, and the mass of the primary body m_1 is fixed at $P_1 = (-\mu, 0, 0)$. The Jacobi constant Γ is then defined by the convention $\Gamma := -2H$. The Hamiltonian H is invariant under the anti-symplectic involutions

$$\begin{aligned} \rho &: (q_1, q_2, q_3, p_1, p_2, p_3) \mapsto (q_1, -q_2, -q_3, -p_1, p_2, p_3), \\ \tilde{\rho} &: (q_1, q_2, q_3, p_1, p_2, p_3) \mapsto (q_1, -q_2, q_3, -p_1, p_2, -p_3), \end{aligned}$$

with corresponding fixed-point loci given by

$$\begin{aligned} L &= \text{Fix}(\rho) = \{q_2 = q_3 = p_1 = 0\}, \\ \tilde{L} &= \text{Fix}(\tilde{\rho}) = \{q_2 = p_1 = p_3 = 0\}. \end{aligned}$$

These correspond respectively to π -rotation around the x -axis, and reflection along the xz -plane. Their composition $\sigma = \rho \circ \tilde{\rho}$ is a symplectic symmetry corresponding to reflection along the xy -plane.

For instance, the *Jupiter–Europa system* then corresponds to a CRTBP with mass ratio $\mu = 2.5266448850435e^{-05}$, and the *Saturn–Enceladus system*, to $\mu = 1.9002485658670e^{-07}$. This information as well as other orbital data can be found in [26] as well as on the webpage <https://ssd.jpl.nasa.gov/sats/>

We shall use this information below.

2.7 Hill’s Lunar Problem

Hill [27] introduced a limit case of the restricted three-body problem as an approach to solve the motion of the Moon in the Sun–Earth problem. As a first approximation, the problem describes the relative motion of two bodies, perturbed by a third, more massive body. The body of interest (Moon) is assumed very close to the smaller primary (Earth) and, by a symplectic rescaling of coordinates, the remaining more massive primary (Sun) is pushed infinitely far away in a way that it acts as a velocity independent gravitational perturbation of the rotating Kepler problem formed by the Earth and the Moon. This problem can therefore be viewed as an approximation to the Saturn–Enceladus and Jupiter–Europa system, when one lets the mass of Europa go to zero. The Hamiltonian describing the system (see 6.3.3 of [28] or 5.8.1 of [29]) is

$$\begin{aligned} E &: (\mathbb{R}^3 \setminus \{0\}) \times \mathbb{R}^3 \rightarrow \mathbb{R}, \\ E(q, p) &= \frac{1}{2} \|p\|^2 - \frac{1}{\|q\|} + p_1 q_2 - p_2 q_1 - q_1^2 + \frac{1}{2} q_2^2 + \frac{1}{2} q_3^2. \end{aligned}$$

The linear symmetries of this problem have been completely characterized [30]. While the planar restricted three-body problem is invariant under reflection at the x -axis, the planar Hill lunar problem is additionally invariant under reflection at the y -axis. For the spatial lunar problem, there are more symmetries: $\rho, \tilde{\rho}$ (which extend the reflection at the x -axis), and two additional symmetries $\kappa, \tilde{\kappa}$ (π -rotation along the

y -axis, and reflection along the yz -plane; both extend the reflection along the y -axis). Their composition is also $\sigma = \kappa \circ \tilde{\kappa}$.

3 Algorithm for Computing Cz-Indices

In this section we propose an algorithm to numerically compute the CZ-index, based on the definition of the CZ-index due to Salamon and Zehnder [31]. An implementation is part of the supplementary material and can be found at <https://github.com/ovkoert/cz-index>

We start with the goals and some intuition before getting down to the definition and computations; the CZ-index of Hamiltonian orbit is a kind of a winding number of the linearized flow along that orbit.

To remove the vagueness in this definition we need some linear algebra and topology. Consider a path of symplectic matrices $\psi : [0, T] \rightarrow Sp(2n)$, for $T > 0$, where $Sp(2n)$ denotes the symplectic group, i.e.

$$Sp(2n) = \{A \in M_{2n \times 2n}(\mathbb{R}) \mid A^t \Omega_{2n} A = \Omega_{2n}\}, \text{ with } \Omega_{2n} = \begin{pmatrix} 0 & \mathbb{1}_n \\ -\mathbb{1}_n & 0 \end{pmatrix}.$$

These are the matrices preserving the symplectic form $\omega(v, w) = v^t \Omega_{2n} w$. Assume that the path ψ starts at the identity and is non-degenerate, meaning that the endpoint $\psi(T)$ has no eigenvalues equal to 1. We want to define the CZ-index μ_{CZ} as the weighted number of times the path ψ goes through the eigenvalue 1. While this can be done and makes the relation with bifurcations clearer, we choose an equivalent approach which is computationally simpler to implement. First define the Maslov cycle as the set of symplectic matrices with eigenvalue 1, so

$$V = \{A \in Sp(2n) \mid \det(A - \mathbb{1}_{2n}) = 0\}.$$

Remark 3.1 The Maslov cycle plays the role of the space of reduced monodromies that are degenerate, and the CZ-index counts the number of degenerate monodromies that lies between the starting point of a periodic orbit and its end point.

The Maslov cycle V divides $Sp(2n)$ into two components, namely

$$C_+ = \{A \in Sp(2n) \mid \det(A - \mathbb{1}_{2n}) > 0\} \text{ and } C_- = \{A \in Sp(2n) \mid \det(A - \mathbb{1}_{2n}) < 0\}.$$

We choose the base points

$$B_+ = \text{diag}(-1, -1, \dots, -1, -1) \in C_+, \text{ and } B_- = \text{diag}(2, 1/2, -1, -1, \dots, -1, -1) \in C_-.$$

We know from the polar decomposition that any symplectic matrix A can be written as $A = US$, where U is unitary and S is a symmetric, positive definite matrix. The unitary part can be extracted using the retract $\rho : Sp(2n) \rightarrow U(n) \subset Sp(2n)$,

$$\rho(A) = (AA^T)^{-1/2} A. \tag{3.3}$$

We can write

$$\rho(A) = \begin{pmatrix} X & -Y \\ Y & X \end{pmatrix}, \tag{3.4}$$

so $X + iY$ is a standard $U(n)$ matrix. Note that for $n = 1$ we can identify $U(1)$ with the circle \mathbb{S}^1 via

$$R_\theta = \begin{pmatrix} \cos \theta & -\sin \theta \\ \sin \theta & \cos \theta \end{pmatrix} \mapsto e^{i\theta}.$$

Observe that $\rho(B_-) = \text{id}$ and $\rho(B_+) = -\text{id}$. Extend ψ to a path $\tilde{\psi} : [0, 2T] \rightarrow Sp(2n)$ such that

- $\tilde{\psi}|_{[T, 2T]}$ does not intersect the Maslov cycle; and
- $\tilde{\psi}(2T) \in \{B_+, B_-\}$.

In other words, simply connect $\psi(T)$ to B_+ if $\psi(T) \in C_+$ with a path in C_+ . Similarly if $\psi(T) \in C_-$. Hence we get a path in the circle $\mathbb{S}^1 = U(1)$ by considering the map

$$\gamma : t \mapsto \det_{\mathbb{C}}(\rho \circ \tilde{\psi}(t)),$$

where $\det_{\mathbb{C}}$ denotes the complex determinant: given a $2n \times 2n$ -matrix in block form (3.4), we define $\det_{\mathbb{C}} \rho(A) = \det(X + iY)$. For example $\det_{\mathbb{C}} R_\theta = e^{i\theta}$. The resulting path γ is not always a loop as it can end in 1 or -1 , but it will be if we double its speed. That gives us the CZ-index by taking the degree of this loop, so

$$\mu_{\text{CZ}}(\psi) = \text{deg}(\det_{\mathbb{C}}(\rho \circ \tilde{\psi}(t))^2). \tag{3.5}$$

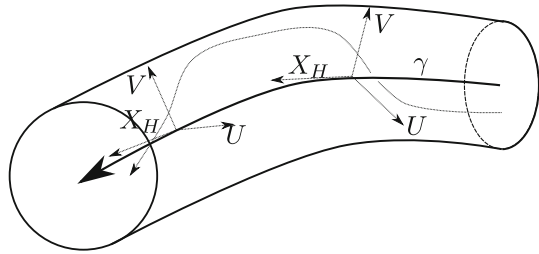
Here, recall that, intuitively, the degree of a map $\gamma : [0, T] \rightarrow \mathbb{S}^1$ taking values in the circle is the number of times it winds around the circle. So the CZ-index as defined above basically counts the number of *half*-turns of the map γ around the circle.

3.1 Trivializations

We now need to connect the above linear algebra to Hamiltonian dynamics. Suppose that H is a time-independent Hamiltonian defined on a phase space, say $M = \mathbb{R}^{2n}$, and consider a periodic orbit γ of the Hamiltonian vector field X_H . We need to choose “yard sticks” with respect to which we measure the rotation of the linearized flow of X_H as sketched in Fig. 9. This is a *symplectic trivialization* or *frame* along the orbit γ , which simply consists of a symplectic basis of the tangent space at each point of the orbit.

For the purpose of computing the CZ-index, we need a trivialization of a specific type we describe now. If we order coordinates as $(q_1, \dots, q_n; p_1, \dots, p_n)$ (this gives a sign for the matrix representation of ω), then we take for each point in the orbit γ , the vectors

Fig. 9 Winding of the linearized flow along an orbit with respect to a frame



$$Z = \frac{1}{\|\nabla H\|^2} \nabla H, \quad X_H = \Omega_{2n} \nabla H.$$

These vectors are normalized to ensure that $\omega(Z, X_H) = dH(Z) = \|\nabla H\|^2 / \|\nabla H\|^2 = 1$, so they form a symplectic frame of $L = \langle Z, X_h \rangle$. For the path of reduced monodromies we need to choose a symplectic basis of the symplectic complement

$$L^\omega = \{Y : \omega(X, Y) = 0 \text{ for } X \in L\}.$$

In full generality, we assume that γ is the boundary of a disk in M (a *spanning* disk). Then there is, by general theory, a symplectic trivialization, which is unique up to deformation. In particular, we can choose a symplectic basis $U_1, V_1, \dots, U_{n-1}, V_{n-1}$ of L^ω .

In our particular situation, things are simpler as we can define a global trivialization, for which quaternionic matrices are useful and give a clean description. Let I, J and K denote the quaternionic matrices. For coordinates (q_1, q_2, p_1, p_2) , this means that

$$I = \begin{pmatrix} 0 & 0 & -1 & 0 \\ 0 & 0 & 0 & -1 \\ 1 & 0 & 0 & 0 \\ 0 & 1 & 0 & 0 \end{pmatrix}, \quad J = \begin{pmatrix} 0 & -1 & 0 & 0 \\ 1 & 0 & 0 & 0 \\ 0 & 0 & 0 & 1 \\ 0 & 0 & -1 & 0 \end{pmatrix}, \quad K = \begin{pmatrix} 0 & 0 & 0 & -1 \\ 0 & 0 & 1 & 0 \\ 0 & -1 & 0 & 0 \\ 1 & 0 & 0 & 0 \end{pmatrix}. \tag{3.6}$$

Note that the first quaternion I corresponds to minus the symplectic matrix, and that $\nabla H, I\nabla H, J\nabla H, K\nabla H$ form orthogonal directions. The last three are all tangent to the energy hypersurface. The first two span L , and we can see that

$$U_1 = \frac{1}{-\|\nabla H\|^2} J\nabla H, \quad V_1 = K\nabla H$$

form a symplectic trivialization of the complement L^ω (keeping the coordinate order in mind). This symplectic trivialization can be deformed into one that extends over the collision locus if we were to consider a regularization scheme such as Levi-Civita regularization and this property guarantees the correct behavior. In particular, this trivialization works for the *planar* CRTBP and for convex Hamiltonians as well. For

the *spatial* CR3BP, we add vectors U_2 and V_2 pointing in the q_3 and p_3 direction, then project the U_1, U_2, V_1, V_2 vectors to make them tangent to the energy hypersurface and then apply the symplectic Gram–Schmidt process to obtain a symplectic trivialization. This way we know that the constructed trivialization coincides with the trivialization used for the planar problem if we restrict. Let us now make this procedure completely explicit. First we define the 6-dimensional variants of the J and K matrices,

$$J_3 = \begin{pmatrix} 0 & -1 & 0 & 0 & 0 & 0 \\ 1 & 0 & 0 & 0 & 0 & 0 \\ 0 & 0 & 0 & 0 & 0 & 0 \\ 0 & 0 & 0 & 0 & 1 & 0 \\ 0 & 0 & 0 & -1 & 0 & 0 \\ 0 & 0 & 0 & 0 & 0 & 0 \end{pmatrix}, \quad K_3 = \begin{pmatrix} 0 & 0 & 0 & 0 & -1 & 0 \\ 0 & 0 & 0 & 1 & 0 & 0 \\ 0 & 0 & 0 & 0 & 0 & 0 \\ 0 & -1 & 0 & 0 & 0 & 0 \\ 1 & 0 & 0 & 0 & 0 & 0 \\ 0 & 0 & 0 & 0 & 0 & 0 \end{pmatrix}. \quad (3.7)$$

We now carry out the above procedure and find

$$Z = \frac{1}{\|\nabla H\|^2} \nabla H,$$

$$U_1 = \frac{1}{-(J_3 \nabla H)^T \Omega_6 K_3 \nabla H} J_3 \nabla H,$$

The formulas for U_2 and V_2 are more unpleasant, so we give the computational procedure. To see that these are the right signs, keep the coordinate ordering in mind.

$$\begin{aligned} U_2 &\leftarrow (0, 0, 0; 0, 0, 1) \\ U_2 &\leftarrow U_2 - (\nabla H^T U_2) Z \\ U_2 &\leftarrow U_2 + (Z^T \Omega_6 U_2) X_H \\ U_2 &\leftarrow U_2 + (U_1^T \Omega_6 U_2) V_1 \\ U_2 &\leftarrow U_2 - (V_1^T \Omega_6 U_2) U_1 \end{aligned}$$

The implementation performs these steps even more explicitly without any simplification. Now that we have symplectic bases of both L_x and L_x^ω at a point x , we define the symplectic frames

$$\begin{aligned} \bar{F}(x) &= (Z \ U_1 \ \dots \ U_{n-1} \ X_H \ V_1 \ \dots \ V_{n-1}) \in Sp(2n) \text{ and} \\ F(x) &= (U_1 \ \dots \ U_{n-1} \ V_1 \ \dots \ V_{n-1}) \in Mat_{2n \times (2n-2)}. \end{aligned}$$

The second frame is simply obtained by projecting out the Z and X_H directions, and will be used to get the reduced monodromy. If $x(t)$ is an orbit with linearized flow $M(x(t))$, then we form the full monodromy path as

$$\Psi(t) = \Omega_{2n}^T \bar{F}(x(t))^T \Omega_{2n} M(x(t)) \bar{F}(x(0)).$$

The path of reduced monodromies is then obtained by projecting out the Z and X_H -directions,

$$\Psi^{red}(t) = \Omega_{2n-2}^T F(x(t))^T \Omega_{2n} M(x(t)) F(x(0)). \tag{3.8}$$

We will define the transverse CZ-index of the orbit γ as the CZ-index of the path $t \mapsto \Psi^{red}(t)$, i.e. $\mu_{CZ}(\gamma, \epsilon) := \mu_{CZ}(\Psi^{red})$. This is then the CZ-index of the orbit γ , which depends only on the homotopy class of trivialization. This means that the index is invariant under continuous deformations of trivializations.

3.2 Pseudocode

We split the computation in steps. In the first step we compute the transverse path using a symplectic trivialization. Correctness of this simple algorithm follows directly from (3.8).

After obtaining the transverse path, we compute the CZ-index; we use an additional function for the construction of a path extension. Implementation of Algorithm 1 is straightforward with a good integrator. In our implementation, we have used the Taylor integrator Heyoka [32], for its accuracy. We will discuss the more technical path extension function in the next section, and focus on Algorithm 2, which computes the CZ-index of a path of symplectic matrices. The basic strategy is to follow the construction from the beginning of Sect. 3, but rather than directly applying (3.3), we compute the retraction to $U(n)$ by the singular value decomposition. To see how this works, we take the singular decomposition $U\Sigma V$ of ψ , and verify

$$(\psi\psi^T)^{-1/2}\psi = (U\Sigma VV^T\Sigma U^T)^{-1/2}U\Sigma V = UV.$$

The reason for using the singular value decomposition is its greater numerical stability. To get a path in $U(1)$, we use the special block structure of the $R(t)$ matrices. If ψ is a $2n \times 2n$ -matrix, then $R = \rho(\psi)$ lies in $O(2n) \cap U(n)$ and has the following block form

$$R = \begin{pmatrix} R_{11} & -R_{21} \\ R_{21} & R_{11} \end{pmatrix}.$$

Combing the blocks, we get the complex $n \times n$ matrix $R_{11} + iR_{21}$ whose determinant c lies in $U(1)$, which is the unit circle in the complex plane. A discretization of the path ψ gives rise to a discretization of the points on the unit circle, so we can simply sum up the angle changes to get the full angle change. In view of Formula (3.5), we double this angle change and divide by 2π to get the winding number. Simplifying we get the following algorithm.

Data: Initial position $x_0 \in \mathbb{R}^{2n}$ of a (non-degenerate) periodic orbit with period $T > 0$.

Result: Reduced monodromy path along the periodic orbit $x : [0, T] \rightarrow \mathbb{R}^{2n}$.

Set initial condition to $x(0) = x_0, M(0) = \mathbb{1}_{2n}$;

Choose a discretization $0 = t_0 < \dots < t_m = T < t_{m+1} < \dots < t_{2m} = 2T$;

Compute linearized flow $x(t), M(t)$ for $t = t_0, \dots, t_m$;

Set $\Psi^{red}(t) \leftarrow \Omega_{2n-2}^T F(x(t))^T \Omega_{2n} M(t) F(x(0))$ for $t = t_0, \dots, t_m$;

Return $\Psi^{red}(t)$ for $t = t_0, \dots, t_m$.

Algorithm 1 Algorithm to obtain transverse path

Data: Discretized path of symplectic matrices.

Result: CZ-index of this path.

Extend discretization $0 = t_0 < \dots < t_m = T$ to $0 = t_0 < \dots < t_m = T < t_{m+1} < \dots < t_{2m} = 2T$;

if $\psi(T) \in C^+$ **then**

$\psi(t) \leftarrow \text{path}(\psi(T), B_+, t)$ for $t = t_m, \dots, t_{2m}$;

else

if $\psi(T) \in C^-$ **then**

$\psi(t) \leftarrow \text{path}(\psi(T), B_-, t)$ for $t = t_m, \dots, t_{2m}$;

end

end

for $t = t_0, \dots, t_{2m}$ **do**

 set $U(t), \Sigma(t), V(t) \leftarrow \text{SVD}(\psi(t))$;

 set $R(t) \leftarrow U(t)V(t)$;

 set $c(t) \leftarrow \det(R_{11}(t) + iR_{21}(t))$;

 Retract to $U(n) \subset SO(2n)$

 Get path in $U(1)$

end

$a \leftarrow 0$;

for $i = 0, \dots, 2m - 1$ **do**

$a \leftarrow a + \arg(c(t_{i+1})/c(t_i)) = a + \text{im}(\log(c(t_{i+1})/c(t_i)))$;

end

return $\text{round}(a/\pi)$

Algorithm 2 CZ-index of path of symplectic matrices

Here $t \rightarrow \text{path}(\psi(T), B_{\pm}, t)$ is a path connecting $\psi(T)$ to B_{\pm} , while avoiding the Maslov cycle. This extension path is described in the next section. Mathematically, the constructed path is continuous, lies in the symplectic group and the extension part

of the path doesn't intersect the Maslov cycle. However, the discretizations of both the numerical approximation and the extension have to be fine enough for the numerical result to be correct. Our implementation takes care of this, by providing criteria to check this. The simplest and most important criteria are described by the following functions:

```

1 def check_symplecticity(s_path):
2     return [np.sum(np.abs(A.transpose() @ Omega4 @ A - Omega4)) for A in
3             ↪ s_path]
4
5 def check_maslov_intersections(s_path):
6     return [maslov_func(s_path[i+1]) * maslov_func(s_path[i]) for i in
7             ↪ range(len(s_path) - 1)]
8
9 def check_continuity(s_path):
10    return [np.sum(np.abs(s_path[i+1] - s_path[i])) for i in
11           ↪ range(len(s_path) - 1)]
12
13 def compute_angular_index(cdets, T):
14    angle_jumps = [np.imag(np.log(cdets[i+1] / cdets[i])) for i in
15                  ↪ range(T-1)]
16    return int(np.round(np.sum(angle_jumps) / np.pi)), angle_jumps

```

The first function checks whether the path is really symplectic by measuring a matrix norm of the defect, which should be small. The second function checks whether the Maslov cycle is crossed; this should not occur in the extension, but can happen if the stepsize is too large. The third function computes a matrix norm of the change of the symplectic path; the changes should be sufficiently small relative to the value of the Maslov function $A \mapsto \det(A - \text{id})$. The last function is used to compute the size of the angle changes, each given by the term $\text{im}(\log(c(t_{i+1})/c(t_i)))$, of the contracted path; the stepsizes should be chosen so small that the angle changes are less than π , otherwise it is not possible to determine in which direction the linearized flow is turning; the angle jumps are returned in the second returned item; the first returned item is the CZ-index. The implementation reports a summary of these norms and jumps, and gives a warning when the jumps are too large. Cases where we found that a finer discretization was necessary, include orbits that come very close to collision, and orbits that are almost degenerate. Although our implementation uses fixed stepsize for simplicity, efficiency can be greatly improved by using adaptive stepsizes.

3.3 Extending the Transverse Path to the Base Point

The extension is based on the following theorem and observations.

Theorem A *The characteristic polynomial of a symplectic matrix $A \in Sp(2n)$ is palindromic, i.e. there are a_0, \dots, a_n such that*

$$\Delta(\lambda) = \lambda^{2n} \Delta\left(\frac{1}{\lambda}\right) = \lambda^n \sum_{k=0}^n a_k (\lambda^k + \lambda^{-k}).$$

Furthermore, if λ is an eigenvalue of A , then so are λ^{-1} , $\bar{\lambda}$ and $\bar{\lambda}^{-1}$.

This means that the eigenvalues of a non-degenerate symplectic matrix come in the following types:

- (\mathcal{E}) A pair of complex conjugate eigenvalues on the unit circle, i.e. an *elliptic* pair;
- (\mathcal{H}^+) A pair of positive real eigenvalues $a, 1/a$, i.e. a *positive hyperbolic* pair;
- (\mathcal{H}^-) A pair of negative real eigenvalues $a, 1/a$, i.e. a *negative hyperbolic* pair;
- (\mathcal{C}) A tuple of four complex eigenvalues $\lambda, 1/\lambda, \bar{\lambda}, 1/\bar{\lambda}$ that are not real and do not lie on the unit circle, i.e. a *complex quadruple*;

For the planar CR3BP, a path corresponding to the reduced monodromy will consist of $Sp(2)$ -matrices. In case the path is non-degenerate, then the endpoint will be one of the following types:

- (\mathcal{E}) or (\mathcal{H}^-) : we connect to B_+ and the index is odd;
- (\mathcal{H}^+) : we connect to B_- and the index is even.

In the spatial CR3BP, a path corresponding to the reduced monodromy will be in $Sp(4)$. The following cases occur for the endpoint:

- (A) $(\mathcal{E}^2), (\mathcal{E}\mathcal{H}^-), (\mathcal{H}^-), (\mathcal{H}^{++}), (\mathcal{C})$: we connect to B_+ and the index is even;
- (B) $(\mathcal{E}\mathcal{H}^+), (\mathcal{H}^{+-})$: we connect to B_- and the index is odd.

Let us explain how to obtain the extension $\tilde{\psi}$ in the spatial case:

- (1) Eliminate all elliptic pairs;
- (2) Eliminate all negative hyperbolic pairs;
- (3) If the endpoint S is of (\mathcal{H}^{++}) type, then take an eigenvalue decomposition $S = BDB^{-1}$, where D is diagonal. The eigenvalues are generically in the form $\lambda, \mu, 1/\lambda, 1/\mu$, where $\lambda \neq \mu$. We can rescale the columns of B such that they become orthogonal with respect to ω . Indeed, if $Sv = \lambda v$ and $Sw = \mu w$, with v, w the columns of B , then

$$\lambda\mu v^t \Omega_4 w = v^t S^t \Omega_4 Sw = v^t \Omega_4 w,$$

so $\omega(v, w) = 0$, since $\lambda\mu \neq 1$. With this in mind:

- First deform the eigenvalues to the form $2, 2, 1/2, 1/2$ by interpolating D to D' ;
- Then rotate $BD'B^{-1}$ to $BR_s D' B^{-1}$ via a continuous path of rotations R_s , so that the end point is of (\mathcal{C}) type.

- (4) If the type is now (C), then connect to B_+ by interpolating the eigenvalues. This finishes case (A).
- (5) If we are in case (B), then after the previous steps we have reduced the matrix to a diagonalizable symplectic matrix whose eigenvalues are a positive hyperbolic pair and eigenvalue -1 with multiplicity 2. By the previous observation, we may write

$$S = BDB^{-1},$$

where B is a symplectic matrix and D is diagonal. With the Iwasawa decomposition, we can write $B = KAN$, where $K \in U(n)$ is unitary, and A, N have the form

$$A = \begin{pmatrix} D' & 0 \\ 0 & D'^{-1} \end{pmatrix}$$

with $D' \in M_{2 \times 2}(\mathbb{R})$ diagonal and positive, and

$$N = \begin{pmatrix} N & M \\ 0 & N^{-t} \end{pmatrix},$$

with N upper triangular with diagonal elements equal to 1, $NM^t = MN^t$. The matrices K, A and N can then be interpolated to the identity. The paper of Benzi and Razouk [33], contains an efficient and simple to implement algorithm, which we have used.

4 Numerical Work

4.1 Result I: Planar Direct/Prograde Orbits

Hénon [34] describes a family g of planar direct periodic orbits which are invariant with respect to both reflections at the x and y -axis. This family undergoes a non-

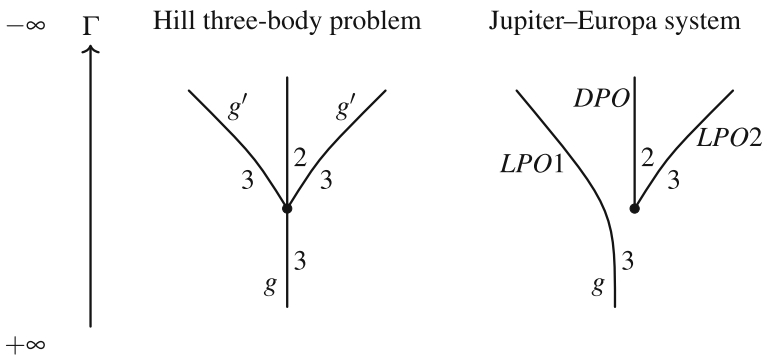


Fig. 10 Bifurcation graphs for the planar direct/prograde orbits with CZ-index

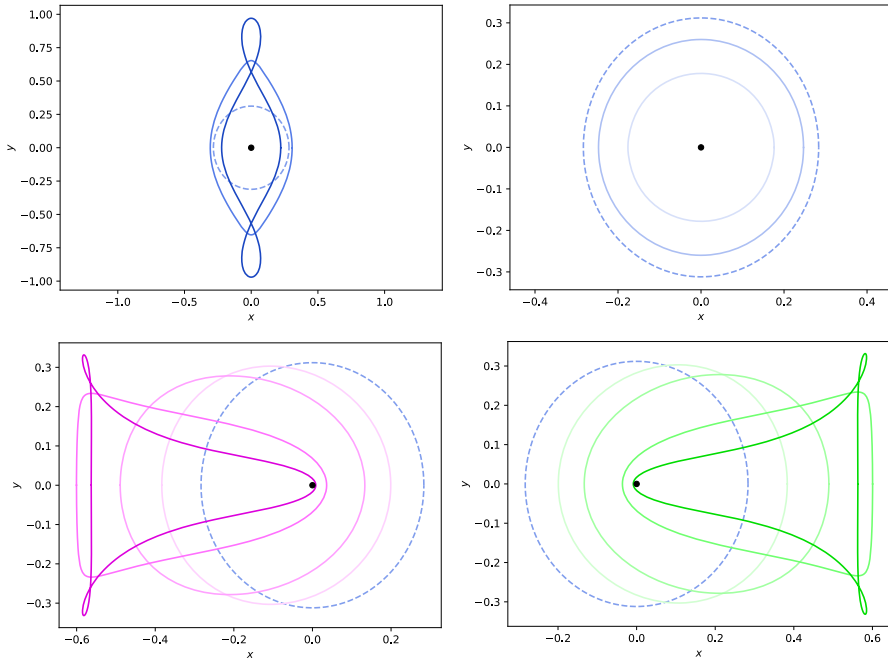


Fig. 11 First row: the g branch whose orbits are in blue and doubly-symmetric w.r.t. the x - and y -axis. From the dashed orbit there bifurcate the two g' branches whose orbits are plotted in the second row and simply-symmetric w.r.t. the x -axis; one g' branch is on the right (the green orbits) and one g' branch is on the left (the purple orbits). From light to dark indicates the increase of the energy in each plot (Color figure online)

generic pitchfork bifurcation, going from elliptic to positive hyperbolic, and where two new families of elliptic orbits, called g' , appear; see the plots in Fig. 11. These new families are still invariant under reflection at the x -axis, but not under reflection at the y -axis. Reflection at the y -axis maps one branch of the g' -family to the other branch. Figure 10 shows the bifurcation graph which is constructed as follows: each vertex denotes a degenerate orbit at which bifurcation happens and each edge represents a family of orbits with varying energy, labeled by the corresponding CZ-index. From this data, it is easy to determine the associated Floer number. For instance in Fig. 10 on the left, the Floer number is $(-1)^3 = -1$ before bifurcation, and $(-1)^2 + 2(-1)^3 = -1$ after bifurcation; they coincide, as they should (Fig. 11).

By deformation, we may go from Hill's lunar problem to the Jupiter–Europa system; see Fig. 10. The pitchfork bifurcation deforms to a *generic* situation, where one of the g' branches glues to the before-bifurcation part of the g branch, the result of which we call the g -LPO1 branch, and where the other g' branch glues to the after-bifurcation part of the g branch, which we call the DPO-LPO2 branch (undergoing birth–death bifurcation). The DPO-orbits are planar positive hyperbolic and the LPO2-orbits are planar elliptic. As the symmetry with respect to the y -axis is lost, the new orbits will be *approximately* symmetric with respect to the y -axis, but not exactly symmetric; similarly, the y -symmetric relation between the g' branches

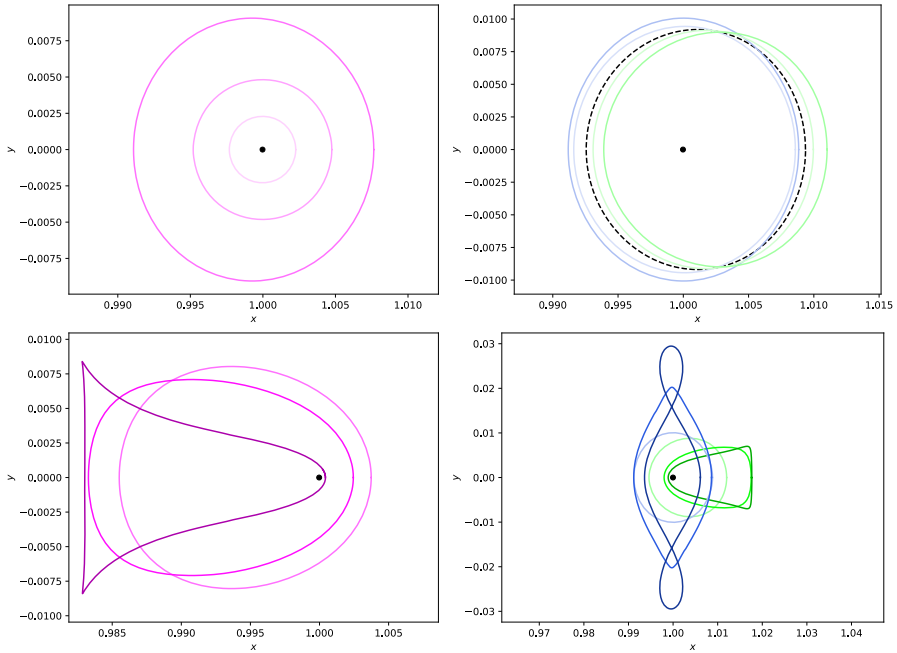


Fig. 12 Left: the g-LPO1 branch in purple, where the energy increases from top to bottom and from light to dark. Right: the DPO-LPO2 branch, split into the DPO sub-branch (left, where orbits are in blue and planar positive hyperbolic) and of the LPO2 sub-branch (right, where orbits are in green and planar elliptic). The black dashed orbit is the degenerate orbit, undergoing birth–death bifurcation (Color figure online)

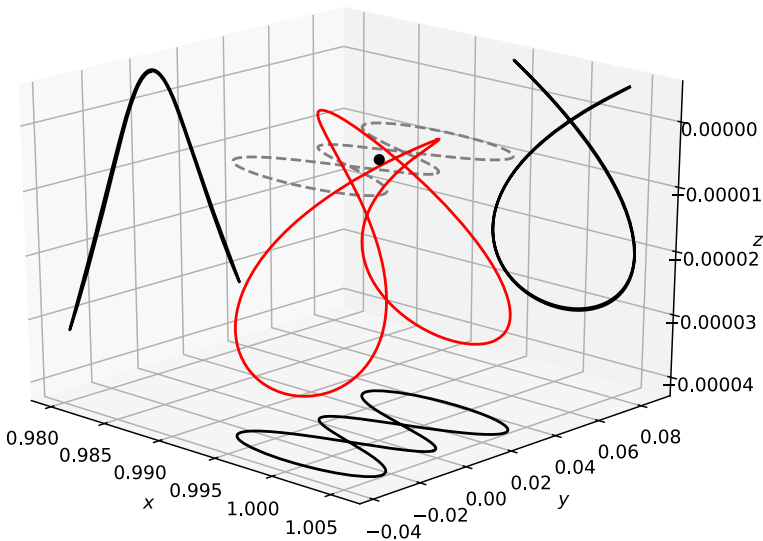


Fig. 13 Jupiter–Europa: A planar-to-spatial bifurcation of a simple closed planar DPO orbit (grey dashed); the reflection at the xy -plane yields its symmetric family

persists only approximately for the corresponding deformed orbits. These families are plotted in Fig. 12, where this behavior is manifest. The data for each new branch is given in Tables 4, 5 and 6 in Appendix B. Via this bifurcation analysis, one may predict the existence of the DPO-LPO2 branch, which a priori is not straightforward to find. While these families are already known and appear e.g., in page 12 of [35], this suggests a general mechanism which we will exploit, cf. Figs. 15, and 16. Note that [35] provides an online data base for *planar* and *x-axis symmetric* periodic orbits, and we match their notation for orbits (DPO, LPO, etc.). The novelty of this article is to focus on *spatial* bifurcations of these planar orbits, employing our novel methods and tools.

4.2 Result II: Bifurcation Graphs with the Same Topology

In the Jupiter–Europa system, the spatial CZ-index of the simple closed DPO-orbit at around $\Gamma = 3.00109352$ jumps by +1, see Table 5 in Appendix B. Therefore it generates a planar-to-spatial bifurcation, see the plot in Fig. 13. As in Hill’s problem, this new family of spatial orbits appears twice by using the reflection at the xy -plane. Surprisingly, compared to Fig. 10, because the symmetry is preserved, the bifurcation graph has the same topology after deformation and is still non-generic, see the graph in Fig. 14.

4.3 Result III: Bifurcation Graphs Between Prograde and Retrograde Orbits

A bifurcation graph relating third covers of g, g' , and fifth covers of planar retrograde orbits, known as family f , was obtained by Aydin [18]; see Fig. 15. The third covers of LPO2 and fifth covers of DRO were found using Cell-Mapping [36]. Taking Fig. 15 as a starting point, we compare it to the Jupiter–Europa system. The result is plotted in Fig. 16.

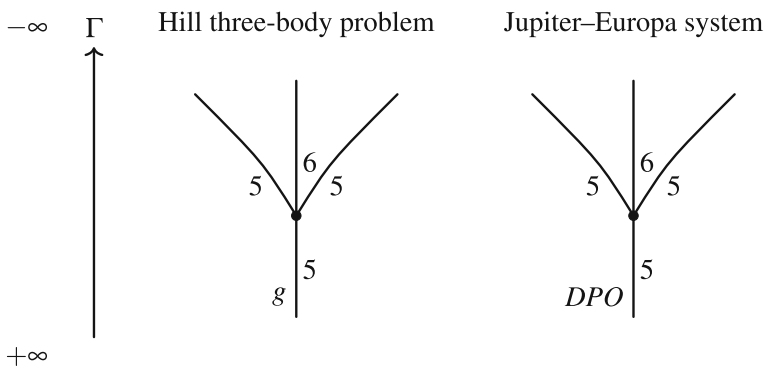


Fig. 14 Left: The bifurcation graph between simple closed g -orbit and the new families of spatial orbits generated by the spatial index jump in Hill’s system. Right: In the Jupiter–Europa system. The horizontal symmetry corresponds to the reflection at the xy -plane

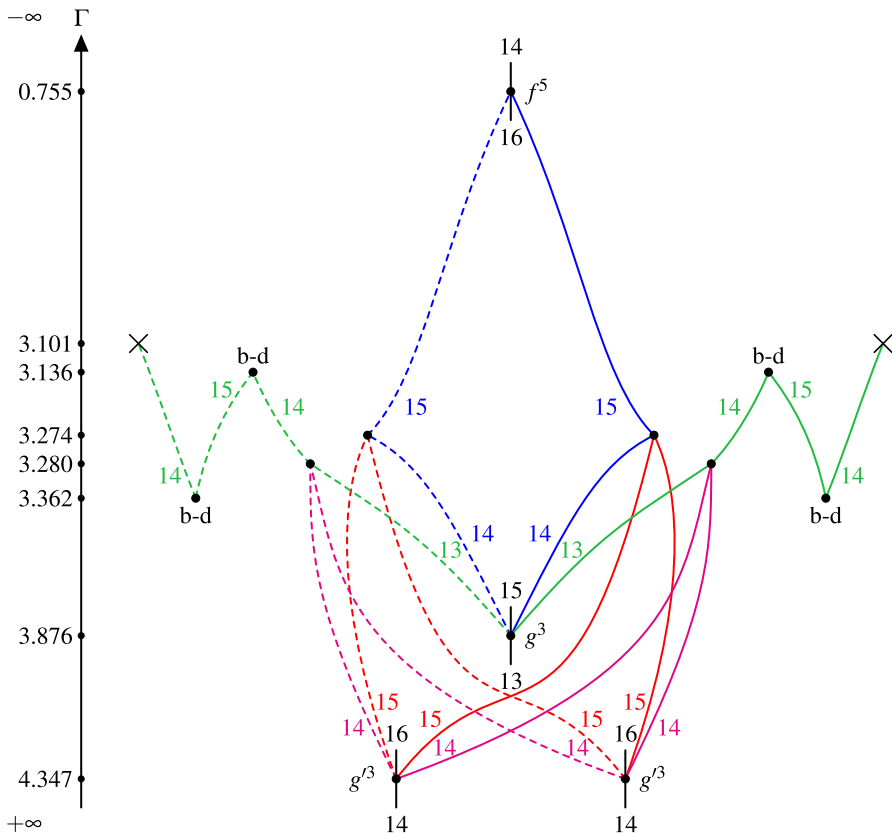


Fig. 15 Bifurcation graph for Hill’s lunar problem by Aydin [18], between the 3rd cover of g , the 3rd cover of g' and the 5th cover of f , based on work of Kalantonis [37]. A cross means collision, and b–d means birth–death bifurcation. The horizontal symmetry in the diagram, relating full and dashed edges, means that the corresponding families are related by a symmetry. For instance, the non-dashed red 15 on the right is related by the dashed red 15 on the left by reflection along the xy -plane. The other red 15 families on the left are obtained by applying the extra two spatial symmetries $\kappa, \tilde{\kappa}$. Similarly for the pink 14 families. The blue and green families are doubly symmetric; one of the symmetries breaks at bifurcation, where the red and pink families appear (Color figure online)

Let us focus on the two unlabeled vertices on the right of Fig. 15 which are not of birth–death type. After deformation, the (red) family starting at g'^3 on the right of CZ-index 15 glues to the (blue) family of the same index ending in f^5 , resolving the vertex at which they meet; note that similarly as in Result I, f is replaced with DRO, and g' , with LPO2. The two other families meeting at the same vertex coming from g'^3 and g^3 now glue to a family undergoing birth–death, where now g' is replaced by g -LPO1, and g , with DPO. A similar phenomenon happens at the other vertex, where the (pink) family starting at g'^3 with CZ-index 14 on the right glues to the (green) family of the same index, and the other two families now undergo birth–death. These families might have been hard to find without this analysis.

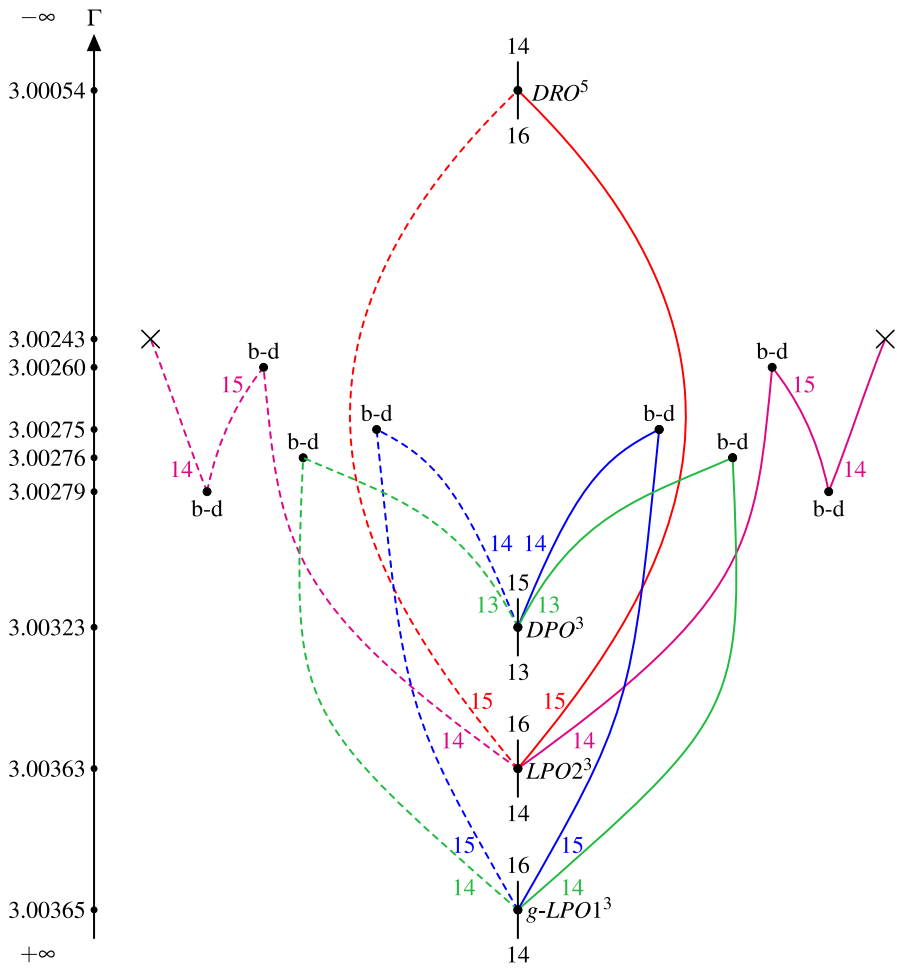


Fig. 16 Bifurcation graph for the Jupiter–Europa system, between $g-LPO1^3$, DPO^3 , $LPO2^3$, and DRO^5 . The data for the pink family is collected in Table 8, for the red one in Table 9, for the blue one in Table 10 and for the green in Table 11. Some orbits of the blue and green family are plotted in Fig. 17. The horizontal symmetry is reflection along the xy -plane. Note that non-dashed red 15 and non-dashed blue 15 are no longer related by a symmetry (Color figure online)

Another notable feature is the (red) family between $LPO2^3$ and DRO^5 of CZ-index 15. This is a *spatial* family connecting two *planar* orbits, one of which is retrograde (DRO^5), and the other, prograde ($LPO2^3$). This family is plotted in Fig. 18.

4.4 Result IV: Bifurcation Graph for Saturn–Enceladus

The periodic orbits in the Saturn–Enceladus system were found by continuation in the μ -parameter, and its bifurcation graph corresponding to the one shown in Fig. 16 has exactly the same topology (but different energy values); it is plotted in Fig. 19.

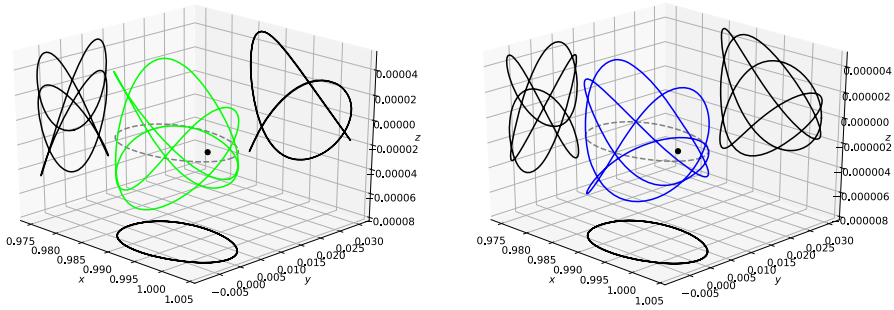


Fig. 17 Jupiter–Europa: Two families of spatial orbits branching out from the $g\text{-}LPO1^3$ orbit (grey dashed); right: these orbits are symmetric w.r.t. the x -axis and their data is collected in Table 10. This is the (blue) family of CZ-index 15 in Fig. 16; left: these orbits are symmetric w.r.t. the xz -plane and their data is collected in Table 11. This is the (green) family of CZ-index 14 in Fig. 16 (Color figure online)

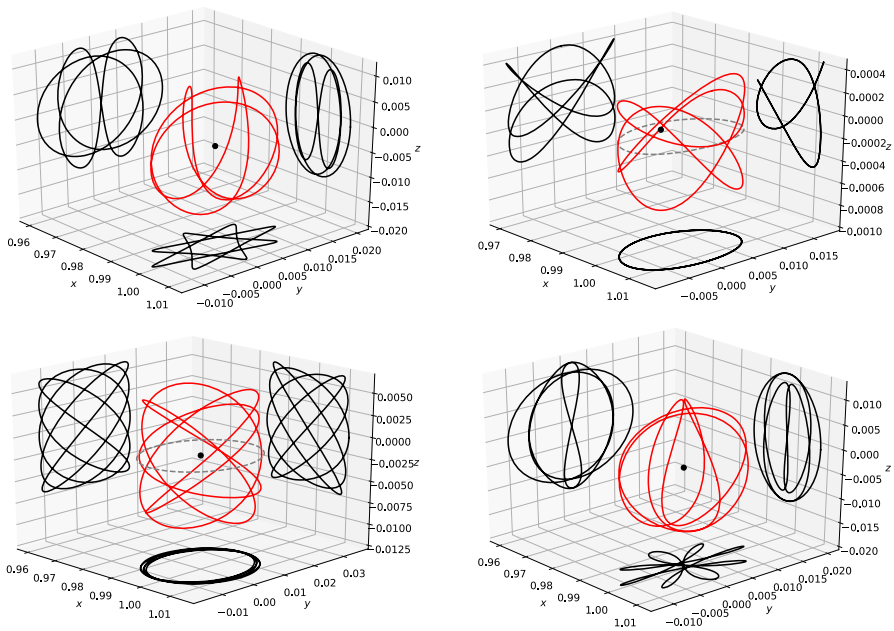


Fig. 18 The red prograde to retrograde spatial connection, with constant CZ-index 15. It starts at the top right where the grey dashed orbit is an LPO2, and the red family bifurcates from its third cover. Its continuation is on the left and then at the bottom from right to left, where on the last the family ends at the fifth cover of planar retrograde orbit (grey dashed) (Color figure online)

Figure 20 gives a bifurcation graph corresponding to the pink families of Fig. 19 (but drawn upside down). Note that it is not only topological, as we also record the starting value along the z axis. The corresponding families of orbits are plotted in Fig. 21.

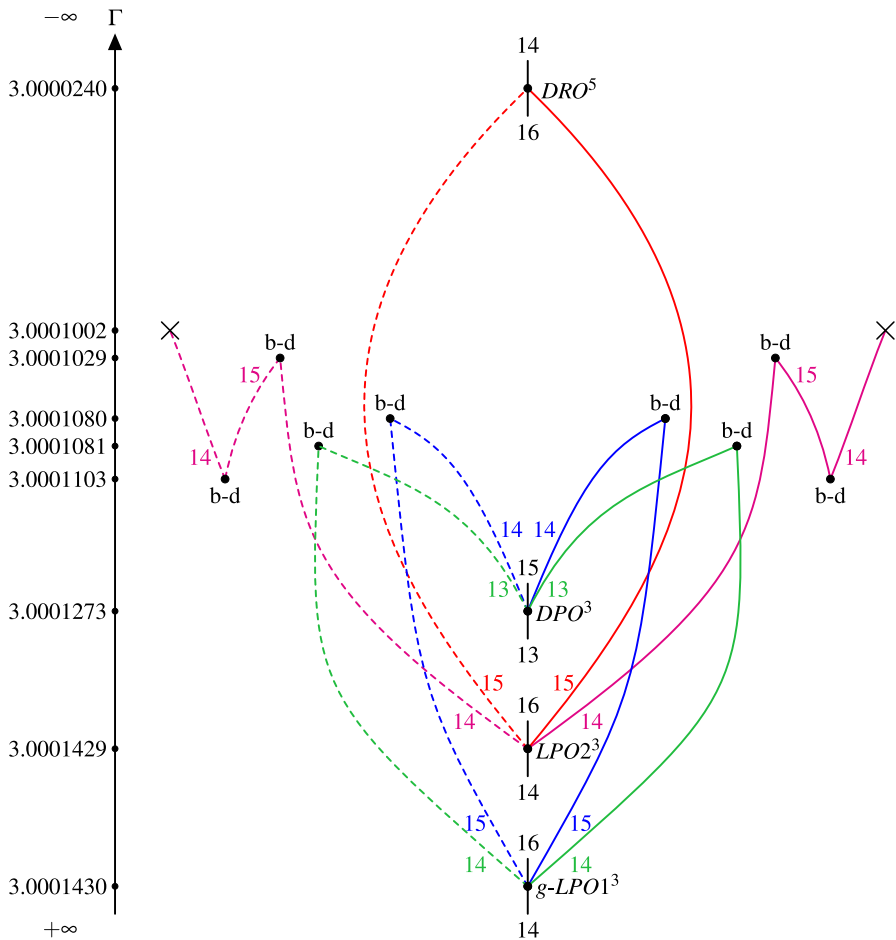


Fig. 19 Bifurcation graph for Saturn–Enceladus. Its topology is exactly the same as that of Fig. 16, but with different energy values (Color figure online)

5 Conclusion

We presented a toolkit extracted from the general methods of symplectic geometry, aimed at studying periodic orbits of Hamiltonian systems, with their bifurcations in families, eigenvalue configurations, and stability, in a visual, and resource-efficient way. In the presence of symmetry, the information attached to orbits, and the methods involved, may be significantly refined. We illustrated these methods on numerical examples, for systems of current interest which are modelled by a restricted three-body problem (Jupiter–Europa, Saturn–Enceladus). We studied families of planar to spatial bifurcations, via bifurcation analysis and deformation from the Hill’s lunar problem. The numerical findings are in agreement with the theoretical predictions, and the bifurcation graphs are completely novel. Appendix A yields an orbit in the

Fig. 20 A bifurcation graph for Saturn–Enceladus of xz -plane symmetric orbits, which corresponds to the pink families in Fig. 19. Horizontal axis is z starting value. Vertical axis is energy (Color figure online)

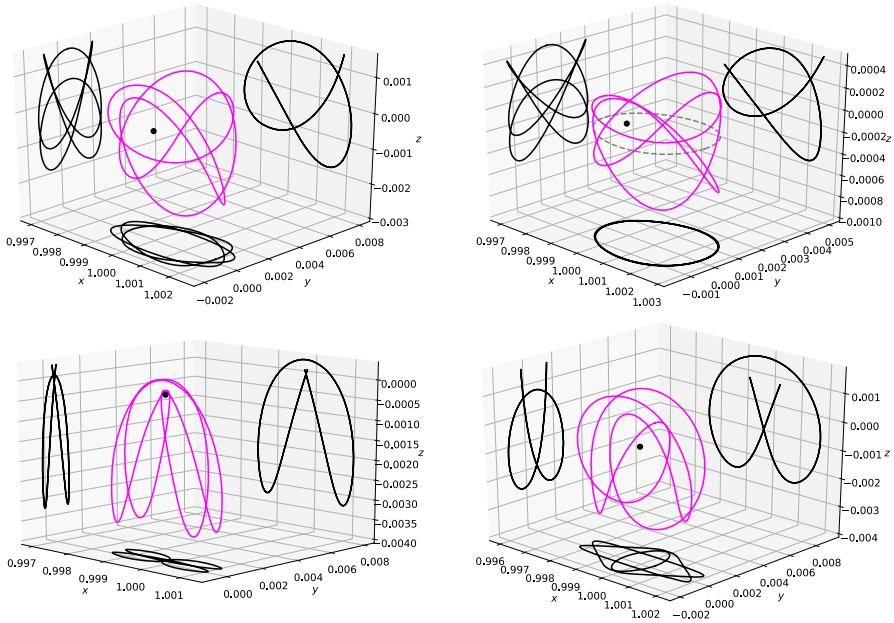
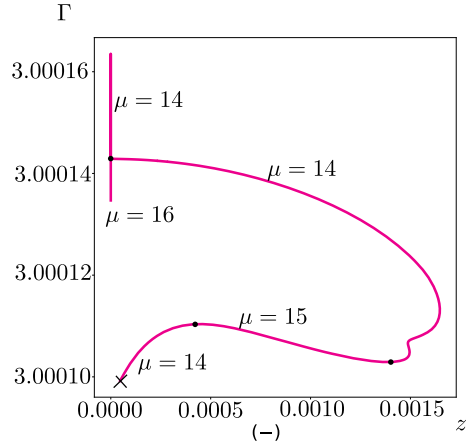


Fig. 21 Plots of the orbits represented by the bifurcation graph of Fig. 20. It starts at the top right where the grey dashed orbit is an LPO2, and the pink family bifurcates from its third cover. Its continuation is on the left and then from the second row from right to left (Color figure online)

Saturn–Enceladus system which approaches the plumes at an altitude of 29 km, and therefore may be used for future missions.

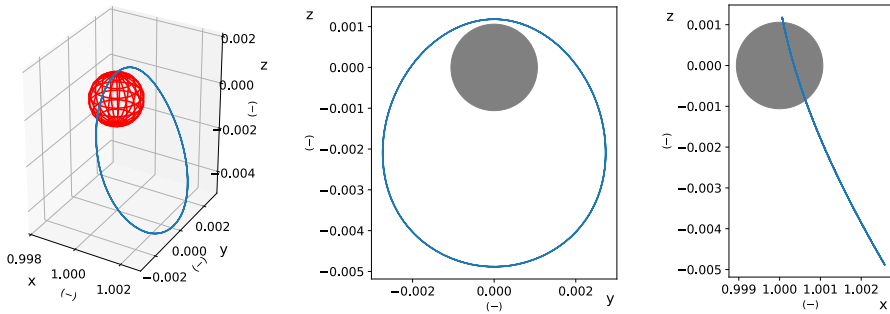


Fig. 22 Plots of a Halo-polar orbit ($\Gamma = 3.000034709155895$) with an altitude of 29 km in the RTBP model for Saturn–Enceladus. The units are normalized, so distance Saturn–Enceladus is set to 1. The Conley–Zehnder index has just jumped to 4, and the type is (\mathcal{E}^2). Enceladus is displayed in red and gray (Color figure online)

Table 1 Halo 2 family to polar near bifurcation for Saturn–Enceladus

Γ	$x(0)$	$z(0)$	Distance to surface (km)	Angle ($^\circ$)	μ_{CZ}
3.0000347723579006	1.0026629054297493	-0.004864325835487838	47	14	3
3.0000347323578973	1.0026358028989037	-0.004870378097113008	42	12	3
3.000034706717895	1.0025922078191964	-0.004879135320319407	33	10	3
3.000034709155895	1.0025751548678687	-0.004882249068671777	29	10	4
3.000034719155896	1.0025570306848521	-0.004885374862351879	25	9	4
3.0000349743579013	1.0024341077005268	-0.004902014803197094	0.6	4	4

Appendix A: Halo Orbits and Polar Orbits

We apply the same methods to the family of Halo orbits coming out of L_2 in the Saturn–Enceladus system. It turns out that this family gets very close to the plumes; the same family appears also in the whitepaper on the Enceladus Orbilander [38]. We continue this family of periodic orbits past a birth–death degeneracy to connect it to the family of polar orbits, compute the indices as well as the distance to the surface at the minimal angle with the pole. We have taken 237,948 km for the semi-major axis of the orbit of Enceladus around Saturn, and 252.1 km for the radius of Enceladus to compute the distance to the surface. The most interesting part of the family occurs just after the index change from 3 to 4, where the orbit is both stable and getting close to the surface as illustrated in Fig. 22 (Tables 1, 2, and 3).

The orbit can of course be continued further as a polar orbit, but this will result in a physical collision.

Table 2 Covers of the Halo 2-polar family for Saturn–Enceladus

Γ	$x(0)$	$z(0)$	Alt (km)	μ_{CZ}^1	μ_{CZ}^2	μ_{CZ}^3	μ_{CZ}^4	μ_{CZ}^5	μ_{CZ}^6	μ_{CZ}^7
3.000034706955895	1.0025846322278920	-0.004880539573622809	31	4	6	10	12	14	18	20
3.0000348143579023	1.0024923126366045	-0.0048950794296966837	12	4	6	10	12	14	18	22

We look at the first up to 7th cover of the Halo orbit: the sevenfold cover shows an index jump

Table 3 Orbit data of the displayed orbit

Γ	$x(0)$	$z(0)$	Alt (km)
3.000034757415899	1.0024991770058109	-0.0048974554261678876	14

Fig. 23 A zoomed view of a periodic orbit coming out of the sevenfold cover of the Halo orbit: orbit data is displayed in Table 3

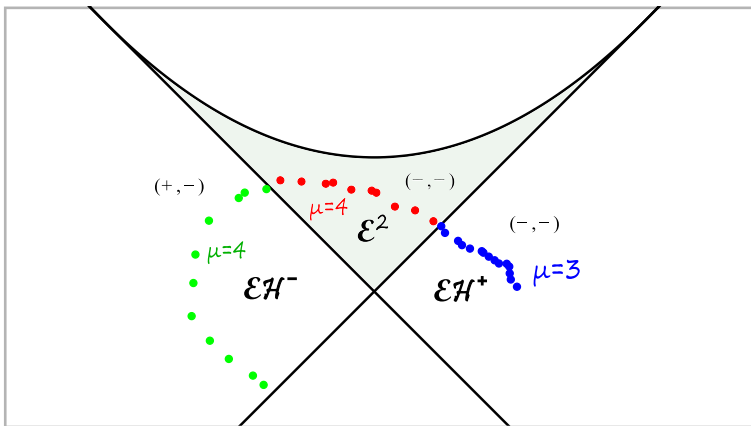
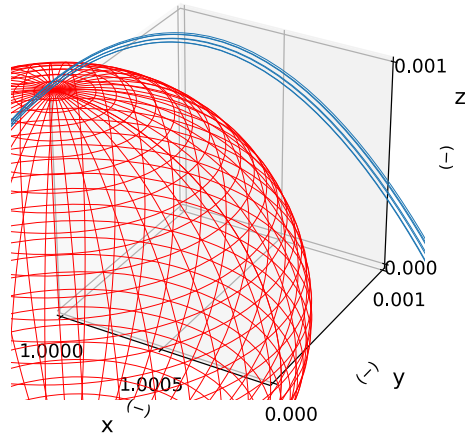


Fig. 24 A GIT plot of the family of Halo orbits, with their corresponding CZ-index. The bifurcation from blue to red is of birth–death type, and from red to green, a period-doubling (Color figure online)

As the sevenfold cover of the Halo orbit makes a jump in index from 20 to 22 as indicated in Table 2, we deduce by invariance of local Floer homology that there must be periodic orbits of index 20 and 21 to compensate. These can then be found by a search nearby the sevenfold cover. One of the orbits, both of which hug the sevenfold cover of the Halo orbit closely, is shown in Fig. 23. The seven strands have a maximal distance of 0.8km from each other. Many more bifurcations of a similar

type occur, but most of the resulting orbits collide with Enceladus. For reference, see the GIT-Broucke stability diagram in Fig. 24, which shows how the family crosses the stable region from side to side, and therefore crosses every rational line; this means that *every* cover bifurcates at some value of the parameter.

Appendix B: Tables

In this appendix, we give tables with the data associated to the various families we have considered (Tables 4, 5, 6, 7, 8, 9, 10, 11, 12, 13, 14, 15, 16, 17, 18, and 19).

Table 4 Data for *g-LPO1* branch for JE

Γ	$x(0)$	$y(0)$	T	(C/B)-sign & Floquet multipliers	$\mu_{CZ}^p / \mu_{CZ}^s / \mu_{CZ}$
3.01142113	1.0226290	0.10284894	0.13999	(+/-) $\varphi_p = 0.137, (\pm)$ $\varphi_s = 0.142$	3 / 3 / 6
3.00383366	1.00797270	0.05073828	1.17402	(+/-) $\varphi_p = 0.332, (\pm)$ $\varphi_s = 1.290$	3 / 3 / 6
3.00372747	1.00538715	0.07480305	1.33771	(+/-) $\varphi_p = 0.556, (\pm)$ $\varphi_s = 1.572$	3 / 3 / 6
3.00365597	1.00378076	0.09779235	1.59835	(+/-) $\varphi_p = 1.068, (\pm)$ $\varphi_s = 2.089$	3 / 3 / 6
3.00360358	1.00244635	0.12945606	2.08332	(+/-) $\varphi_p = 1.845, (\pm)$ $\varphi_s = 3.136$	3 / 3 / 6
3.00360326	1.00243628	0.12977936	2.08832	(+/-) $\varphi_p = 1.858, (+/+)$ $\lambda_s = -1.03$	3 / 3 / 6
3.00360049	1.00234732	0.13271728	2.13332	(+/-) $\varphi_p = 1.987, (+/+)$ $\lambda_s = -1.05$	3 / 3 / 6
3.00359960	1.00231829	0.13370950	2.14831	(+/-) $\varphi_p = 2.037, (\mp)$ $\varphi_s = 3.166$	3 / 3 / 6
3.00358255	1.00180287	0.15481646	2.43323	(+/+) $\lambda_p = -4.39, (\mp)$ $\varphi_s = 3.796$	3 / 3 / 6
3.00343430	1.00043030	0.32769866	3.13136	(+/+) $\lambda_p = -129, (\mp)$ $\varphi_s = 5.223$	3 / 3 / 6

Table 5 Data for *DPO* branch for JE

Γ	$x(0)$	$y(0)$	T	(C/B)-sign & Floquet multipliers	$\mu_{CZ}^p / \mu_{CZ}^s / \mu_{CZ}$
3.00374605	1.00900895	0.04460670	1.25362	(-/-) $\lambda_p = 1.29, (\pm)$ $\varphi_s = 1.385$	2 / 3 / 5
3.00358658	1.00884026	0.04739922	1.41448	(-/-) $\lambda_p = 2.23, (\pm)$ $\varphi_s = 1.565$	2 / 3 / 5
3.00356924	1.00889026	0.04727261	1.43426	(-/-) $\lambda_p = 2.36, (\pm)$ $\varphi_s = 1.589$	2 / 3 / 5
3.00340053	1.00928559	0.04673515	1.64653	(-/-) $\lambda_p = 4.29, (\pm)$ $\varphi_s = 1.829$	2 / 3 / 5
3.00323697	1.00958786	0.04684116	1.88433	(-/-) $\lambda_p = 8.52, (\pm)$ $\varphi_s = 2.094$	2 / 3 / 5
3.00257321	1.00913170	0.05562606	2.88768	(-/-) $\lambda_p = 136, (\pm)$ $\varphi_s = 3.092$	2 / 3 / 5
3.00237147	1.00863170	0.05990199	3.16288	(-/-) $\lambda_p = 246, (\mp)$ $\varphi_s = 3.334$	2 / 3 / 5
3.00109352	1.00470170	0.09778837	5.12979	(-/-) $\lambda_p = 2485, (\mp)$ $\varphi_s = 6.161$	2 / 3 / 5
3.00109192	1.00469670	0.09785369	5.13303	(-/-) $\lambda_p = 2570, (+/+)$ $\lambda_s = 1.027$	2 / 4 / 6
3.00107109	1.00463170	0.09871030	5.17546	(-/-) $\lambda_p = 3062, (+/+)$ $\lambda_s = 1.540$	2 / 4 / 6

Table 6 Data for *LPO2* branch for JE

Γ	$x(0)$	$y(0)$	T	(C/B)-sign & Floquet multipliers	$\mu_{CZ}^p / \mu_{CZ}^s / \mu_{CZ}$
3.00374885	1.00955895	0.04118756	1.25694	(+/-) $\varphi_p = 0.190, (\pm)$ $\varphi_s = 1.397$	3 / 3 / 6
3.00371150	1.01150895	0.03105844	1.34143	(+/-) $\varphi_p = 0.538, (\pm)$ $\varphi_s = 1.555$	3 / 3 / 6
3.00369790	1.01200895	0.02882949	1.37591	(+/-) $\varphi_p = 0.625, (\pm)$ $\varphi_s = 1.620$	3 / 3 / 6
3.00363027	1.01440084	0.01977091	1.62295	(+/-) $\varphi_p = 1.101, (\pm)$ $\varphi_s = 2.094$	3 / 3 / 6
3.00357414	1.016776	0.0130372	2.1215	(+/-) $\varphi_p = 1.878, (\pm)$ $\varphi_s = 3.131$	3 / 3 / 6
3.00357388	1.016787	0.013014	2.12519	(+/-) $\varphi_p = 1.885, (+/+)$ $\lambda_s = -1.02$	3 / 3 / 6
3.00356878	1.01701395	0.01253366	2.20708	(+/-) $\varphi_p = 2.120, (\mp)$ $\varphi_s = 3.225$	3 / 3 / 6
3.00353952	1.01771395	0.01187914	2.65553	(+/+) $\lambda_p = -9.64, (\mp)$ $\varphi_s = 4.144$	3 / 3 / 6
3.00349789	1.01765259	0.01364657	2.95454	(+/+) $\lambda_p = -36.3, (\mp)$ $\varphi_s = 4.743$	3 / 3 / 6

Table 7 Data for *DRO* branch for JE

Γ	$x(0)$	$y(0)$	T	(C/B)-sign & Floquet multipliers	$\mu_{CZ}^p / \mu_{CZ}^s / \mu_{CZ}$
3.00429783	0.99502455	0.07670173	0.40998	(-/+) $\varphi_p = 5.862, (\mp)$ $\varphi_s = 5.894$	1 / 1 / 2
3.00156431	0.99037034	0.06224607	1.02778	(-/+) $\varphi_p = 5.245, (\mp)$ $\varphi_s = 5.406$	1 / 1 / 2
3.00101739	0.98833167	0.06026263	1.32856	(-/+) $\varphi_p = 4.973, (\mp)$ $\varphi_s = 5.216$	1 / 1 / 2
3.00060753	0.98623049	0.05949811	1.64998	(-/+) $\varphi_p = 4.712, (\mp)$ $\varphi_s = 5.050$	1 / 1 / 2
3.00054882	0.98587513	0.05946574	1.7052	(-/+) $\varphi_p = 4.670, (\mp)$ $\varphi_s = 5.026$	1 / 1 / 2
2.99962388	0.97762100	0.06369886	3	(-/+) $\varphi_p = 4.001, (\mp)$ $\varphi_s = 4.787$	1 / 1 / 2
2.99935885	0.97409965	0.06735824	3.5	(-/+) $\varphi_p = 3.987, (\mp)$ $\varphi_s = 4.863$	1 / 1 / 2
2.99908502	0.97038828	0.07212000	4	(-/+) $\varphi_p = 3.995, (\mp)$ $\varphi_s = 5.001$	1 / 1 / 2
2.99868251	0.96488658	0.08024713	4.6003	(-/+) $\varphi_p = 4.185, (\mp)$ $\varphi_s = 5.254$	1 / 1 / 2

Table 8 Data for one branch bifurcation from 3rd cover of the *LPO2*-orbit for JE

Γ	$x(0)$	$z(0)$	$y(0)$	T	(C/B)-sign & Floquet multipliers	μ_{CZ}
3.00363027	1.01440084	0	0.01974709	4.86	(-/+) $\varphi_p^3 = 3.305, \varphi_s^3 = 0$	14 \rightarrow 16
3.00362881	1.01439256	0.00046114	0.01976648	4.87	(-/+) $\varphi_1 = 3.300, (\mp)$ $\varphi_2 = 6.281$	14
3.00359018	1.01415816	0.00242577	0.02031752	4.90	(-/+) $\varphi_1 = 3.208, (\mp)$ $\varphi_2 = 6.280$	14
3.00357914	1.01409052	0.00273476	0.02047842	4.91	(+/-) $\lambda = -1.05, (\mp)$ $\varphi = 6.278$	14
3.00354287	1.01386628	0.003555363	0.02101794	4.94	(+/-) $\lambda = -1.18, (\mp)$ $\varphi = 6.255$	14
3.00325974	1.01198527	0.00688259	0.02594794	5.2	(+/-) $\lambda = -1.62, (\mp)$ $\varphi = 5.963$	14
3.00298774	1.00985792	0.00824897	0.03258269	5.5	(+/-) $\varphi_1 = 2.566, (\mp)$ $\varphi_2 = 5.657$	14
3.00270453	1.00652898	0.00795347	0.04651756	5.85	(-/+) $\varphi_1 = 1.947, (\mp)$ $\varphi_2 = 5.978$	14
3.00264234	1.00560524	0.00778449	0.05051319	5.88	(+/-) $\lambda = -1.09, (\mp)$ $\varphi = 5.958$	14
3.00263168	1.00544296	0.00774780	0.05124733	5.88	(-/+) $\varphi_1 = 3.488, (\mp)$ $\varphi_2 = 5.937$	14

Table 8 continued

Γ	$x(0)$	$z(0)$	$\dot{y}(0)$	T	(C/B)-sign & Floquet multipliers	μ_{CZ}
3.00260038	1.00454296	0.00720347	0.05686831	5.86	(-/+) $\varphi_1 = 4.662, (\mp)$ $\lambda = 1$	b-d
3.00260927	1.00399399	0.00658371	0.06201856	5.8	(-/+) $\varphi = 4.813, (+/+)$ $\lambda = 2.278$	15
3.00266582	1.00306075	0.00521508	0.07465765	5.6	(-/+) $\varphi = 4.443, (+/+)$ $\lambda = 3.660$	15
3.00278841	1.00150186	0.00269606	0.11584022	5	(-/+) $\varphi = 3.653, (+/+)$ $\lambda = 1.829$	15
3.00279353	1.00129733	0.00238127	0.12512611	4.9	(-/+) $\varphi_1 = 3.540, (\mp)$ $\lambda = 1$	b-d
3.00277937	1.00084704	0.00169978	0.15351993	4.66	(-/+) $\varphi_1 = 3.246, (\mp)$ $\varphi_2 = 5.702$	14

These spatial orbits are simply-symmetric w.r.t. the xz -plane and ends at collision. Its symmetric family is obtained by using the reflection at the xy -plane

Table 9 Data for one branch bifurcation from $LPO2^3$ -orbit for JE, ending at DRO^5

Γ	$x(0)$	$\dot{y}(0)$	$\dot{z}(0)$	T	(C/B)-sign & Floquet multipliers	μ_{CZ}
3.00363027	1.01440084	0.01974709	0	4.86	(-/+) $\varphi_p^3 = 3.305, \varphi_s^3 = 0$	14 \rightarrow 16
3.00351924	1.01408954	0.01928185	0.01342237	4.96	(-/-) $\lambda_1 = -1.24, (-/-)$ $\lambda_2 = 1.09$	15
3.00321170	1.01314307	0.01799332	0.02676988	5.25	(-/-) $\lambda_1 = -1.62, (-/-)$ $\lambda_2 = 1.45$	15
3.00302231	1.01246670	0.01723541	0.03300118	5.46	(+/-) $\varphi = 2.749, (-/-)$ $\lambda = 1.78$	15
3.00273486	1.01099334	0.01657953	0.04285920	5.82	(+/-) $\varphi = 1.618, (-/-)$ $\lambda = 1.55$	15
3.00270684	1.01077857	0.01644568	0.04412031	5.85	(+/-) $\varphi = 1.801, (-/-)$ $\lambda = 1.40$	15
3.00266563	1.01548137	0.01548137	0.04575934	5.88	(+/-) $\varphi = 2.506, (-/-)$ $\lambda = 1.35$	15
3.00243536	1.01068879	0.00516070	0.04995370	6	(-/+) $\varphi = 5.761, (-/-)$ $\lambda = 8.52$	15
3.00204821	1.01119864	-0.01174966	0.05089250	6.24	(-/+) $\varphi = 5.965, (-/-)$ $\lambda = 31.1$	15
3.00172312	1.01167768	-0.02457421	0.04793350	6.5	(-/+) $\varphi = 6.016, (-/-)$ $\lambda = 30.0$	15
3.00147493	1.01207539	-0.03349482	0.04374826	6.75	(-/+) $\varphi = 6.070, (-/-)$ $\lambda = 22.3$	15
3.00127220	1.01242785	-0.04020652	0.03910792	7	(-/+) $\varphi = 6.124, (-/-)$ $\lambda = 15.2$	15
3.00096072	1.01304236	-0.04944170	0.02947258	7.5		15

Table 9 continued

Γ	$x(0)$	$\dot{y}(0)$	$\dot{z}(0)$	T	(C/B)-sign & Floquet multipliers	μ_{CZ}
					(-/+) $\varphi = 6.201, (-/-)$ $\lambda = 6.16$	
3.00073221	1.01358551	-0.05528744	0.01932635	8	(-/+) $\varphi = 5.911, (-/-)$ $\lambda = 1.14$	15
3.00055690	1.01409401	-0.05914769	0.00388381	8.5	(-/+) $\varphi = 4.550, (-/-)$ $\lambda = 1.00$	15
3.00054882	1.01412064	-0.05930512	0	8.52	(-/+) $\varphi_p^5 = 4.500, \varphi_s^5 = 0$	16 \rightarrow 14

The CZ-index is constant, and gives a bridge between the planar orbits. These spatial orbits are x -axis-symmetric. Its symmetric family is obtained by reflection at the ecliptic

Table 10 Data for one branch bifurcation from $g-LPO1^3$ for JE

Γ	$x(0)$	$\dot{y}(0)$	$\dot{z}(0)$	T	(C/B)-sign & Floquet multipliers	μ_{CZ}
3.00365597	0.98557900	-0.01951876	0	4.79	(-/+) $\varphi_p^3 = 3.205, \varphi_s^3 = 0$	14 \rightarrow 16
3.00365338	0.98556744	-0.01945341	0.00182488	4.80	(-/+) $\varphi = 3.214, (-/-)$ $\lambda = 1.001$	15
3.00363389	0.98561874	-0.01938011	0.00580611	4.82	(-/-) $\lambda_1 = -1.01, (-/-)$ $\lambda_2 = 1.005$	15
3.00329911	0.98657072	-0.01815373	0.02416862	5.12	(-/-) $\lambda_1 = -1.54, (-/-)$ $\lambda_2 = 1.378$	15
3.00314093	0.98708523	-0.01763006	0.02950246	5.30	(-/-) $\lambda_1 = -1.02, (-/-)$ $\lambda_2 = 1.685$	15
3.00300399	0.98759083	-0.01727225	0.03377964	5.46	(+/-) $\varphi = 2.290, (-/-)$ $\lambda = 1.977$	15
3.00281046	0.98856773	-0.01745284	0.04009001	5.73	(+/-) $\varphi = 0.976, (-/-)$ $\lambda = 2.451$	15
3.00275889	0.98918471	-0.01885469	0.04265726	5.82	(+/-) $\varphi = 0.134, (-/-)$ $\lambda = 4.422$	15
						b-d
3.00275823	0.98925887	-0.01917383	0.04284561	5.82	(-/-) $\lambda_1 = 1.041, (-/-)$ $\lambda_2 = 5.013$	14
3.00276196	0.98939330	-0.01992825	0.04305515	5.83	(-/-) $\lambda_1 = 1.148, (-/-)$ $\lambda_2 = 6.636$	14
3.00296320	0.98997681	-0.03157520	0.03598567	5.75	(-/-) $\lambda_1 = 1.064, (-/-)$ $\lambda_2 = 100.2$	14
3.00316033	0.99025736	-0.04249067	0.02045809	5.68	(-/-) $\lambda_1 = 1.011, (-/-)$ $\lambda_2 = 400.3$	14
3.00323676	0.99035914	-0.04685850	0.00096495	5.65	(-/-) $\lambda_1 = 1.0001, (-/-)$ $\lambda_2 = 619.3$	14
3.00323697	0.99035942	-0.04686768	0	5.65	$\varphi_s^3 = 0, (-/-)$ $\lambda = 620.23$	13 \rightarrow 15

These spatial orbits are x -axis-symmetric and connected to one branch bifurcation from DPO^3 via b-d. Its symmetric family is obtained by reflection at the ecliptic

Table 11 Data for one branch bifurcation from 3rd cover of the *g-LPO1*-orbit for JE

Γ	$x(0)$	$z(0)$	$\dot{y}(0)$	T	(C/B)-sign & Floquet multipliers	μ_{CZ}
3.00365597	0.98557900	0	-0.01951876	4.79	(-/+) $\varphi_p^3 = 3.205,$ $\varphi_s^3 = 0$	14 → 16
3.00365461	0.98556706	-0.00036219	-0.01947401	4.80	(-/+) $\varphi_1 = 3.215, (\mp)$ $\varphi_2 = 6.281$	14
3.00363389	0.98568597	-0.00175392	-0.01975974	4.82	(+/+) $\lambda = -1.01, (\mp)$ $\varphi = 6.277$	14
3.00360033	0.98588066	-0.00278699	-0.02023321	4.84	(+/+) $\lambda = -1.12, (\mp)$ $\varphi = 6.263$	14
3.00331461	0.98766211	-0.00655464	-0.02492170	5.11	(+/+) $\lambda = -1.52, (\mp)$ $\varphi = 5.978$	14
3.00314742	0.98883839	-0.00763969	-0.02842198	5.29	(+/-) $\varphi_1 = 3.031, (\mp)$ $\varphi_2 = 5.756$	14
3.00289637	0.99094696	-0.00836889	-0.03579903	5.61	(+/-) $\varphi_1 = 1.373, (\mp)$ $\varphi_2 = 5.309$	14
3.00285045	0.99142732	-0.00835072	-0.03776509	5.67	$0.376 \pm 0.570i,$ $0.806 \pm 1.221i$	14
3.00277633	0.99243798	-0.00805049	-0.04244268	5.78	$0.491 \pm 0.121i,$ $1.917 \pm 0.472i$	14
3.00277358	0.99249304	-0.00802039	-0.04284315	5.79	(+/+) $\lambda_1 = 1.987,$ (-/-) $\lambda_2 = 2.016$	14
3.00276770	0.993012244	-0.00750257	-0.04644237	5.82	(+/+) $\lambda_1 = 1.000,$ (-/-) $\lambda_2 = 7.181$	14
						b-d
3.00277093	0.99302677	0.00744432	-0.04668427	5.82	(-/+) $\varphi = 6.138,$ (-/-) $\lambda = 8.013$	13
3.00296373	0.99201168	0.00567451	-0.04755480	5.75	(-/+) $\varphi = 6.233,$ (-/-) $\lambda = 100.3$	13
3.00316033	0.99081340	0.00306250	-0.04704925	5.68	(-/+) $\varphi = 6.263,$ (-/-) $\lambda = 400.3$	13
3.00323697	0.99035942	0	-0.04686768	5.65	(-/-) $\lambda = 620.23,$ $\varphi_s^3 = 0$	13 → 15

These spatial orbits are simply-symmetric w.r.t. the *xz*-plane and they are connected to one branch bifurcation from the 3rd cover of the *DPO*-orbit via birth–death. Its symmetric family is obtained by using the reflection at the ecliptic

Table 12 *g-LPO1* branch for SE

Γ	$x(0)$	$\dot{y}(0)$	T	(C/B)-sign & Floquet multipliers	$\mu_{CZ}^p / \mu_{CZ}^s / \mu_{CZ}$
3.00033109	1.00061213	0.01702742	0.22681	(+/-) $\varphi_p = 0.218, (\pm)$ $\varphi_s = 0.232$	3 / 3 / 6
3.00015209	1.00157026	0.00982528	1.13552	(+/-) $\varphi_p = 0.421, (\pm)$ $\varphi_s = 1.245$	3 / 3 / 6
3.00014609	1.00109981	0.01422219	1.33077	(+/-) $\varphi_p = 0.534, (\pm)$ $\varphi_s = 1.549$	3 / 3 / 6
3.00014309	1.00076095	0.01889960	1.60328	(+/-) $\varphi_p = 1.118, (\pm)$ $\varphi_s = 2.081$	3 / 3 / 6
3.00014089	1.00047925	0.02552883	2.13798	(+/-) $\varphi_p = 1.962, (+/+)$ $\lambda_s = -1.06$	3 / 3 / 6
3.00014069	1.00044659	0.02664172	2.22579	(+/-) $\varphi_p = 2.302, (\mp)$ $\varphi_s = 3.324$	3 / 3 / 6
3.00014049	1.00041446	0.02785333	2.31612	(+/+) $\lambda_p = -1.58, (\mp)$ $\varphi_s = 3.513$	3 / 3 / 6
3.00013817	1.00020619	0.04126365	2.90065	(+/+) $\lambda_p = -35.5, (\mp)$ $\varphi_s = 4.711$	3 / 3 / 6

Table 13 *DPO* branch for SE

Γ	$x(0)$	$\dot{y}(0)$	T	(C/B)-sign & Floquet multipliers	$\mu_{CZ}^p / \mu_{CZ}^s / \mu_{CZ}$
3.00014744	0.99838904	-0.00977411	1.23860	(-/-) $\lambda_p = 1.188, (\pm)$ $\varphi_s = 1.364$	2 / 3 / 5
3.00014064	0.99826971	-0.00934116	1.41906	(-/-) $\lambda_p = 2.270, (\pm)$ $\varphi_s = 1.571$	2 / 3 / 5
3.00012744	0.99811661	-0.00917943	1.88166	(-/-) $\lambda_p = 8.463, (\pm)$ $\varphi_s = 2.091$	2 / 3 / 5
3.00011304	0.99809959	-0.00985129	2.46619	(-/-) $\lambda_p = 46.25, (\pm)$ $\varphi_s = 2.697$	2 / 3 / 5
3.00010524	0.99815786	-0.01051283	2.76504	(-/-) $\lambda_p = 101.1, (\pm)$ $\varphi_s = 2.979$	2 / 3 / 5
3.00008192	0.99846180	-0.01309687	3.59018	(-/-) $\lambda_p = 500.3, (\pm)$ $\varphi_s = 3.699$	2 / 3 / 5
3.00006838	0.99867270	-0.01491712	4.08764	(-/-) $\lambda_p = 911.4, (\pm)$ $\varphi_s = 4.164$	2 / 3 / 5

Table 14 *LPO2* branch for SE

Γ	$x(0)$	$\dot{y}(0)$	T	(C/B)-sign & Floquet multipliers	$\mu_{CZ}^p / \mu_{CZ}^s / \mu_{CZ}$
3.00014639	1.00217453	0.00646333	1.30672	(+/-) $\varphi_p = 0.451, (\pm)$ $\varphi_s = 1.499$	3 / 3 / 6
3.00014319	1.00276240	0.00405869	1.57114	(+/-) $\varphi_p = 1.018, (\pm)$ $\varphi_s = 2.009$	3 / 3 / 6
3.00014299	1.00279991	0.00393120	1.59627	(+/-) $\varphi_p = 1.060, (\pm)$ $\varphi_s = 2.059$	3 / 3 / 6
3.00014075	1.00328757	0.00253817	2.11312	(+/-) $\varphi_p = 1.881, (+/+)$ $\lambda_s = -1.03$	3 / 3 / 6
3.00014061	1.00331899	0.00247078	2.17031	(+/-) $\varphi_p = 2.043, (\mp)$ $\varphi_s = 3.142$	3 / 3 / 6
3.00014030	1.00338269	0.00235356	2.31077	(+/+) $\lambda_p = -1.22, (\mp)$ $\varphi_s = 3.484$	3 / 3 / 6
3.00013613	1.00339866	0.00308260	3.07749	(+/+) $\lambda_p = -69.2, (\mp)$ $\varphi_s = 5.041$	3 / 3 / 6

Table 15 *DRO* branch for SE

Γ	$x(0)$	$\dot{y}(0)$	T	(C/B)-sign & Floquet multipliers	$\mu_{CZ}^p / \mu_{CZ}^s / \mu_{CZ}$
3.00010525	1.00137692	-0.01325298	0.67023	(-/+) $\varphi_p = 5.595, (\mp)$ $\varphi_s = 5.673$	1 / 1 / 2
3.00004405	1.00224224	-0.01182054	1.29643	(-/+) $\varphi_p = 5.001, (\mp)$ $\varphi_s = 5.234$	1 / 1 / 2
3.00002425	1.00276541	-0.01163206	1.70339	(-/+) $\varphi_p = 4.671, (\mp)$ $\varphi_s = 5.027$	1 / 1 / 2
2.99999205	1.00419386	-0.01226462	2.84090	(-/+) $\varphi_p = 4.060, (\mp)$ $\varphi_s = 4.785$	1 / 1 / 2
2.99996645	1.00592895	-0.01421020	4.06771	(-/+) $\varphi_p = 4.007, (\mp)$ $\varphi_s = 5.025$	1 / 1 / 2
2.99995365	1.00682933	-0.01550883	4.56302	(-/+) $\varphi_p = 4.172, (\mp)$ $\varphi_s = 5.236$	1 / 1 / 2
2.99986545	1.01156940	-0.02377257	5.79878	(-/+) $\varphi_p = 5.114, (\mp)$ $\varphi_s = 5.951$	1 / 1 / 2

Table 16 Purple 14 for SE

Γ	$x(0)$	$z(0)$	$\dot{y}(0)$	T	(C/B)-sign & Floquet multipliers	μ_{CZ}
3.00014299	1.00279991	0	0.00393120	4.78	(-/+) $\varphi_p^3 = 3.182, \varphi_s^3 = 0$	14 → 16
3.00014260	1.00281790	0.00019127	0.00386379	4.84	(-/+) $\varphi_1 = 3.259, (\mp)$ $\varphi_2 = 6.282$	14
3.00014129	1.00277804	0.00047538	0.00395858	4.87	(+/+) $\lambda = 3.208, (\mp)$ $\varphi = 6.280$	14
3.00012209	1.00211470	0.00153818	0.00578987	5.36	(+/-) $\varphi_1 = 3.111, (\mp)$ $\varphi_2 = 5.740$	14
3.00010829	1.00137563	0.00156298	0.00875806	5.82	(-/+) $\varphi_1 = 0.776, (\mp)$ $\varphi_2 = 5.669$	14
3.00010291	1.00087722	0.00139401	0.01128814	5.86	(+/-) $\varphi_1 = 4.665, (\mp)$ $\varphi_2 = 6.126$	14
						b-d
3.00010295	1.00083899	0.00135458	0.01162196	5.84	(-/+) $\varphi = 4.783, (+/+)$ $\lambda = 1.517$	15
3.00010612	1.00055789	0.00095022	0.01542803	5.53	(-/+) $\varphi = 4.334, (+/+)$ $\lambda = 3.712$	15
3.00011036	1.00024558	0.00044664	0.02518603	4.86	(-/+) $\varphi = 3.504, (+/+)$ $\lambda = 1.109$	15
						b-d
3.00011031	1.00021998	0.00040764	0.02663091	4.80	(-/+) $\varphi_1 = 3.424, (\mp)$ $\varphi_2 = 5.916$	14
3.00010281	1.00003238	0.00010169	0.05878312	4.17	(-/+) $\varphi_1 = 3.781, (\mp)$ $\varphi_2 = 5.884$	14
3.00010021	1.00001491	0.00006054	0.07739259	4.08	(-/+) $\varphi_1 = 3.965, (\mp)$ $\varphi_2 = 6.041$	14

These spatial orbits are simply-symmetric w.r.t. the xz -plane and ends at collision. Its symmetric family is obtained by using the reflection at the xy -plane

Table 17 Red 15 for SE

Γ	$x(0)$	$\dot{y}(0)$	$\dot{z}(0)$	T	(C/B)-sign & Floquet multipliers	μ_{CZ}
3.00014299	1.00279991	0.00393120	0	4.78	(-/+) $\varphi_p^3 = 3.182, \varphi_s^3 = 0$	14 → 16
3.00013559	1.00272159	0.00369764	0.00343416	5.00	(-/-) $\lambda_1 = -1.39, (-/-)$ $\lambda_2 = 1.13$	15
3.00012559	1.00256280	0.00349797	0.00541943	5.26	(-/-) $\lambda_1 = -1.53, (-/-)$ $\lambda_2 = 1.52$	15
3.00012139	1.00248791	0.00342004	0.00611889	5.38	(+/-) $\varphi = 2.928, (-/-)$ $\lambda = 1.73$	15
3.00011759	1.00241319	0.00335832	0.00672992	5.50	(+/-) $\varphi = 2.395, (-/-)$ $\lambda = 1.90$	15
3.00010399	1.00204385	0.00282460	0.00925842	5.90	(-/+) $\varphi = 3.184, (-/-)$ $\lambda = 1.41$	15

Table 17 continued

Γ	$x(0)$	$\dot{y}(0)$	$\dot{z}(0)$	T	(C/B)-sign & Floquet multipliers	μ_{CZ}
3.00009759	1.00208424	0.00127533	0.00976558	5.98	(-/+) $\varphi = 5.692, (-/-)$ $\lambda = 6.55$	15
3.00009417	1.00210781	0.00047162	0.00992209	6.03	(-/+) $\varphi = 5.846, (-/-)$ $\lambda = 13.5$	15
3.00009145	1.00212691	-0.00015208	0.00999912	6.07	(-/+) $\varphi = 5.888, (-/-)$ $\lambda = 18.8$	15
3.00007425	1.00225503	-0.00382600	0.00970041	6.38	(-/+) $\varphi = 5.974, (-/-)$ $\lambda = 32.3$	15
3.00005185	1.00244477	-0.00788343	0.00765368	7.00	(-/+) $\varphi = 6.092, (-/-)$ $\lambda = 15.2$	15
3.00004205	1.00254154	-0.00938862	0.00615688	7.40	(-/+) $\varphi = 6.171, (-/-)$ $\lambda = 7.51$	15
3.00003105	1.00266948	-0.01085595	0.00374582	8.01	(-/+) $\varphi = 5.829, (-/-)$ $\lambda = 1.08$	15
3.00002425	1.00276636	-0.01162574	0.00034005	8.51	(-/+) $\varphi = 4.510, (-/-)$ $\lambda = 1.05$	15
3.00002405	1.00277176	-0.01163165	0	8.54	(-/+) $\varphi_p^5 = 4.489, \varphi_s^5 = 0$	16 \rightarrow 14

The CZ-index is constant, and gives a bridge between the planar orbits. These spatial orbits are x -axis-symmetric. Its symmetric family is obtained by reflection at the ecliptic

Table 18 Blue 15 and Blue 14 for SE

Γ	$x(0)$	$\dot{y}(0)$	$\dot{z}(0)$	T	(C/B)-sign & Floquet multipliers	μ_{CZ}
3.00014309	0.99718487	-0.00386895	0	4.80	(-/+) $\varphi_p^3 = 3.217, \varphi_s^3 = 0$	14 \rightarrow 16
3.00014289	0.99717670	-0.00383214	0.00048106	4.83	(-/+) $\varphi = 3.246, (-/-)$ $\lambda = 1.016$	15
3.00014169	0.99719319	-0.00380810	0.00145833	4.85	(-/-) $\lambda_1 = -1.04, (-/-)$ $\lambda_2 = 1.027$	15
3.00013425	0.99730021	-0.00365996	0.00377737	5.02	(-/-) $\lambda_1 = -1.45, (-/-)$ $\lambda_2 = 1.183$	15
3.00012251	0.99749232	-0.00343875	0.00594605	5.34	(-/-) $\lambda_1 = -1.03, (-/-)$ $\lambda_2 = 1.700$	15
3.00012093	0.99752153	-0.00341248	0.00620193	5.39	(+/-) $\varphi = 2.758, (-/-)$ $\lambda = 1.782$	15
3.00011193	0.99772535	-0.00333595	0.00766874	5.69	(+/-) $\varphi = 0.976, (-/-)$ $\lambda = 2.451$	15
3.00010800	0.99793026	-0.00365343	0.00862538	5.84	(+/-) $\varphi = 0.092, (-/-)$ $\lambda = 2.549$	15
3.00010820	0.99796166	-0.00381731	0.00868408	5.84	(-/-) $\lambda_1 = 1.196, (-/-)$ $\lambda_2 = 3.812$	14

b-d

Table 18 continued

Γ	$x(0)$	$\dot{y}(0)$	$\dot{z}(0)$	T	(C/B)-sign & Floquet multipliers	μ_{CZ}
3.00010958	0.99799080	-0.00423992	0.00854277	5.83	(-/-) $\lambda_1 = 1.171, (-/-)$ $\lambda_2 = 10.02$	14
3.00012042	0.99807079	-0.00718764	0.00594564	5.71	(-/-) $\lambda_1 = 1.068, (-/-)$ $\lambda_2 = 203.9$	14
3.00012568	0.99810519	-0.00868716	0.00307711	5.66	(-/-) $\lambda_1 = 1.011, (-/-)$ $\lambda_2 = 485.0$	14
3.00012738	0.99811615	-0.00918031	0	5.65	$\phi_s^3 = 0, (-/-)$ $\lambda_p = 620.1$	13 \rightarrow 15

These spatial orbits are x -axis-symmetric and connected to one branch bifurcation from DPO^3 via b–d. Its symmetric family is obtained by reflection at the ecliptic

Table 19 Green 14 and Green 13 for SE

Γ	$x(0)$	$z(0)$	$\dot{y}(0)$	T	(C/B)-sign & Floquet multipliers	μ_{CZ}
3.00014306	0.99718487	0	-0.00386895	4.80	(-/+) $\phi_p^3 = 3.217, \phi_s^3 = 0$	14 \rightarrow 16
3.00014210	0.99720294	0.00036902	-0.00390227	4.84	(-/+) $\phi_1 = 3.197, (\mp)$ $\phi_2 = 6.282$	14
3.00014182	0.99721138	0.00041974	-0.00392247	4.85	(+/+) $\lambda = -1.01, (\mp)$ $\phi = 6.281$	14
3.00013324	0.99748294	0.00114054	-0.00461090	5.05	(+/+) $\lambda = -1.48, (\mp)$ $\phi = 6.089$	14
3.00012084	0.99793674	0.00156551	-0.00595530	5.39	(+/-) $\phi_1 = 2.704, (\mp)$ $\phi_2 = 5.684$	14
3.00011446	0.99822206	0.00164295	-0.00696832	5.60	(+/-) $\phi_1 = 1.776, (\mp)$ $\phi_2 = 5.499$	14
3.00011146	0.99838620	0.00163494	-0.00763914	5.71	$0.458 \pm 0.723i,$ $0.624 \pm 0.986i$	14
3.00010841	0.99863569	0.00153928	-0.00887793	5.82	$0.595 \pm 0.212i,$ $1.489 \pm 0.530i$	14
3.00010824	0.99866658	0.00151731	-0.00906541	5.83	(+/+) $\lambda_1 = 1.448, (-/-)$ $\lambda_2 = 1.786$	14
3.00010818	0.99869599	0.00149114	-0.00926286	5.84	(+/+) $\lambda_1 = 1.034, (-/-)$ $\lambda_2 = 2.566$	14
3.00010852	0.99871851	0.00144710	-0.00949590	5.84	(-/+) $\phi = 6.109, (-/-)$ $\lambda = 4.479$	13
3.00010970	0.99869031	0.00139716	-0.00954957	5.83	(-/+) $\phi = 6.135, (-/-)$ $\lambda = 10.065$	13
3.00011700	0.99844373	0.00110062	-0.00936425	5.75	(-/+) $\phi = 6.253, (-/-)$ $\lambda = 102.96$	13
3.00012680	0.99813343	0.00026518	-0.00918878	5.65	(-/+) $\phi = 6.280, (-/-)$ $\lambda = 572.25$	13

b–d

Table 19 continued

Γ	$x(0)$	$z(0)$	$y'(0)$	T	(C/B)-sign & Floquet multipliers	μ_{CZ}
3.00012738	0.99811615	0	-0.00918031	5.65	$\varphi_s^3 = 0, (-/-) \lambda_p = 620.1$	$13 \rightarrow 15$

These spatial orbits are simply-symmetric w.r.t. the xz -plane and they are connected to one branch bifurcation from the 3rd cover of the *DPO*-orbit via b-d. Its symmetric family is obtained by using the reflection at the ecliptic

Acknowledgements The authors are grateful to the anonymous referees for very thoughtful comments, which have greatly improved the quality of the manuscript. A. Moreno would also like to thank Stefano Campagnola, Martín Lara, Juan Félix San Juan Díaz, Dan Scheeres, Dario Izzo and Rita Mastroianni for insightful discussions throughout the preparation of the work. A. Moreno is currently supported by the Sonderforschungsbereich TRR 191 Symplectic Structures in Geometry, Algebra and Dynamics, funded by the DFG (Projektnummer 281071066 - TRR 191), by the DFG under Germany's Excellence Strategy EXC 2181/1 - 390900948 (the Heidelberg STRUCTURES Excellence Cluster), and by the Air Force Office of Scientific Research (AFOSR) under Award No. FA8655-24-1-7012. O. van Koert was supported by National Research Foundation of Korea Grant NRF2023005562 funded by the Korean Government. C. Aydin acknowledges support by the Deutsche Forschungsgemeinschaft (DFG, German Research Foundation) - Project ID 281071066 - TRR 191 and Project ID 541062288.

Funding Open Access funding enabled and organized by Projekt DEAL.

Open Access This article is licensed under a Creative Commons Attribution 4.0 International License, which permits use, sharing, adaptation, distribution and reproduction in any medium or format, as long as you give appropriate credit to the original author(s) and the source, provide a link to the Creative Commons licence, and indicate if changes were made. The images or other third party material in this article are included in the article's Creative Commons licence, unless indicated otherwise in a credit line to the material. If material is not included in the article's Creative Commons licence and your intended use is not permitted by statutory regulation or exceeds the permitted use, you will need to obtain permission directly from the copyright holder. To view a copy of this licence, visit <http://creativecommons.org/licenses/by/4.0/>.

References

1. Abraham, R., Marsden, J.E.: Foundations of Mechanics, 2nd edn., revised and enlarged, With the assistance of Tudor Rațiu and Richard Cushman. Benjamin/Cummings Publishing Co., Inc., Advanced Book Program, Reading (1978)
2. McDuff, D., Salamon, D.: Introduction to Symplectic Topology. Oxford Graduate Texts in Mathematics, 3rd edn. Oxford University Press, Oxford (2017). <https://doi.org/10.1093/oso/9780198794899.001.0001>
3. Maruskin, J.M.: Dynamical Systems and Geometric Mechanics. De Gruyter Studies in Mathematical Physics. An Introduction, vol. 48, 2nd edn. De Gruyter, Berlin (2018). <https://doi.org/10.1515/9783110597806>
4. Moreno, A.: The symplectic geometry of the three-body problem. arXiv e-prints [arXiv:2101.04438](https://arxiv.org/abs/2101.04438) [math.SG]

5. Audin, M., Damian, M.: Morse Theory and Floer Homology. Universitext. Translated from the 2010 French original by Reinie Ern . Springer, London; EDP Sciences, Les Ulis (2014). <https://doi.org/10.1007/978-1-4471-5496-9>
6. Frauenfelder, U., Moreno, A.: On GIT quotients of the symplectic group, stability and bifurcations of periodic orbits. *J. Symplectic Geom.* (To appear)
7. Broucke, R.: Stability of periodic orbits in the elliptic, restricted three-body problem. *AIAA J.* **7**, 1003 (1969)
8. Moreno, A., Ruscelli, F.: Combinatorics of linear stability for Hamiltonian systems in arbitrary dimension. arXiv e-prints [arXiv:2311.06167](https://arxiv.org/abs/2311.06167) [math.SG] (2023)
9. Frauenfelder, U., Koh, D., Moreno, A.: Symplectic methods in the numerical search of orbits in real-life planetary systems. arXiv e-prints [arXiv:2206.00627](https://arxiv.org/abs/2206.00627) [math.SG]
10. Krein, M.G.: On the application of an algebraic proposition in the theory of matrices of monodromy. *Uspekhi Mat. Nauk (N.S.)* **6.1(41)**, 171–177 (1951)
11. Krein, M.G.: On the theory of entire matrix functions of exponential type. *Ukr. Mat. Zurnal* **3**, 164–173 (1951)
12. Moser, J.: New aspects in the theory of stability of Hamiltonian systems. *Commun. Pure Appl. Math.* **11**, 81–114 (1958). <https://doi.org/10.1002/cpa.3160110105>
13. Conley, C., Zehnder, E.: Morse-type index theory for flows and periodic solutions for Hamiltonian equations. *Commun. Pure Appl. Math.* **37(2)**, 207–253 (1984). <https://doi.org/10.1002/cpa.3160370204>
14. Robbin, J., Salamon, D.: The Maslov index for paths. *Topology* **32(4)**, 827–844 (1993). [https://doi.org/10.1016/0040-9383\(93\)90052-W](https://doi.org/10.1016/0040-9383(93)90052-W)
15. Lara, M., Russell, R., Villac, B.: Classification of the distant stability regions at Europa. *J. Guid. Control Dyn.* (2006). <https://doi.org/10.2514/1.22372>
16. Lara, M., Russell, R.: On the family “g” of the restricted three-body problem. *Monografias de la Real Academia de Ciencias de Zaragoza* **30**, 51–66 (2006)
17. Michalodimitrakis, M.: Hill’s problem: families of three-dimensional periodic orbits (part I). *Astrophys. Space Sci.* **68**, 253–268 (1980)
18. Aydin, C.: The Conley-Zehnder Indices of the spatial Hill three-body problem. *Celest. Mech. Dyn. Astron.* (2023). <https://doi.org/10.1007/s10569-023-10134-7>
19. Lara, M., Juan, S., Juan, F.: Dynamic behavior of an orbiter around Europa. *J. Guid. Control Dyn.* (2005). <https://doi.org/10.2514/1.5686>
20. Hu, X., Sun, S.: Morse index and stability of elliptic Lagrangian solutions in the planar three-body problem. *Adv. Math.* **223(1)**, 98–119 (2010). <https://doi.org/10.1016/j.aim.2009.07.017>
21. Kavle, H., Offin, D., Portaluri, A.: Keplerian orbits through the Conley-Zehnder Index. *Qual. Theory Dyn. Syst.* (2021). <https://doi.org/10.1007/s12346-020-00430-0>
22. Aydin, C.: From Babylonian lunar observations to Floquet multipliers and Conley-Zehnder indices. *J. Math. Phys.* (2023). <https://doi.org/10.1063/5.0156959>
23. Frauenfelder, U., Moreno, A.: On doubly symmetric periodic orbits. *Celest. Mech. Dyn. Astron.* **135** (2), Paper No. 20, 18 (2023). <https://doi.org/10.1007/s10569-023-10135-6>
24. Meyer, K.R.: Generic bifurcation of periodic points. *Trans. Am. Math. Soc.* **149(1)**, 95–107 (1970). <https://doi.org/10.1090/s0002-9947-1970-0259289-x>
25. Szebehely, V.: *Theory of Orbit: The Restricted Problem of Three Bodies*. Elsevier Science (2012)
26. Jaumann, R., et al.: Icy satellites: geological evolution and surface processes. In: Dougherty, M.K., Esposito, L.W., Krimigis, S.M. (eds.) *Saturn from Cassini-Huygens*. Springer, Dordrecht (2009). https://doi.org/10.1007/978-1-4020-9217-6_20
27. Hill, G.W.: On the part of the motion of the lunar perigee which is a function of the mean motions of the sun and moon. *Acta Math.* **8(1)**, 1–36 (1886). <https://doi.org/10.1007/BF02417081>
28. Meyer, K.R., Offin, D.C.: *Introduction to Hamiltonian Dynamical Systems and the N-Body Problem*. Springer International Publishing, Cham (2017). <https://doi.org/10.1007/978-3-319-53691-0>
29. Frauenfelder, U., van Koert, O.: *The Restricted Three-Body Problem and Holomorphic Curves*. Springer International Publishing, Cham (2018). <https://doi.org/10.1007/978-3-319-72278-8>
30. Aydin, C.: The linear symmetries of Hill’s lunar problem. *Arch. Math. (Basel)* **120(3)**, 321–330 (2023). <https://doi.org/10.1007/s00013-022-01822-1>
31. Salamon, D., Zehnder, E.: Morse theory for periodic solutions of Hamiltonian systems and the Maslov index. *Commun. Pure Appl. Math.* **45(10)**, 1303–1360 (1992). <https://doi.org/10.1002/cpa.3160451004>

32. Biscani, F., Izzo, D.: Revisiting high-order Taylor methods for astrodynamics and celestial mechanics. *Mon. Not. R. Astron. Soc.* **504**(2), 2614–2628 (2021). <https://doi.org/10.1093/mnras/stab1032>
33. Benzi, M., Razouk, N.: On the Iwasawa decomposition of a symplectic matrix. *Appl. Math. Lett.* **20**(3), 260–265 (2007). <https://doi.org/10.1016/j.aml.2006.04.004>
34. Hénon, M.: Numerical exploration of the restricted problem. V. Hill's case: periodic orbits and their stability. *Astron. Astrophys.* **1**, 223–238 (1969)
35. Restrepo, R., Russell, R.: A database of planar axi-symmetric periodic orbits for the solar system. In: *AAS/AIAA Astrodynamics Specialist Conference*, AAS 17-694 (2017)
36. Koh, D., Anderson, R., Bermejo-Moreno, I.: Cell-mapping orbit search for mission design at ocean worlds using parallel computing. *J. Astronaut. Sci.* **68**, 172–196 (2021). <https://doi.org/10.1007/s40295-021-00251-6>
37. Kalantonis, V.S.: Numerical investigation for periodic orbits in the Hill three-body problem. *Universe* **6**(6), 72 (2020)
38. MacKenzie, S.M., Kirby, K.W., Greenauer, P.J.: Enceladus Orbilander: A Flagship Mission Concept for Astrobiology. Technical report 20205008712. The Johns Hopkins Applied Physics Laboratory and NASA (2020). <https://ntrs.nasa.gov/citations/20205008712>

Publisher's Note Springer Nature remains neutral with regard to jurisdictional claims in published maps and institutional affiliations.